COMPARISON OF POLYNOMIAL PROFILES AND INPUT SHAPING FOR INDUSTRIAL APPLICATIONS

A Thesis
Presented to
The Academic Faculty

by

Brice Pridgen

In Partial Fulfillment
of the Requirements for the Degree
Master of Science in the
George W. Woodruff School of Mechanical Engineering

Georgia Institute of Technology
May 2011

COMPARISON OF POLYNOMIAL PROFILES AND INPUT SHAPING FOR INDUSTRIAL APPLICATIONS

Approved by:

Professor William Singhose, Advisor
George W. Woodruff School of Mechanical Engineering
Georgia Institute of Technology

Professor Al Ferri
George W. Woodruff School of Mechanical Engineering
Georgia Institute of Technology

Professor Jun Ueda
George W. Woodruff School of Mechanical Engineering
Georgia Institute of Technology

Date Approved: March 17, 2011

ACKNOWLEDGEMENTS

I would like to thank my advisor, Dr. William Singhose, for his patient guidance and inspirational curiosity. He has been a driving force during this time of growth and learning, and I am very appreciative of the opportunities he has provided me with. I would like to acknowledge my colleagues, Kun Bai, Daichi Fujioka, Ehsan Maleki, Kelvin Peng, and James Potter, for their support and assistance over the past 18 months. I would also like to thank Dr. Joshua Vaughan who has been a limitless source of knowledge and direction.

I would like to thank my family for their support throughout my life. Their encouragement has helped open doors to new and exciting experiences. And special thanks to my loving wife, Kelley, who was most accommodating to my grad-student lifestyle.

Finally, I would like to thank my committee members, Dr. Al Ferri and Dr. Jun Ueda, and also Siemens Energy and Automation and Boeing for support of my research.

TABLE OF CONTENTS

LIST OF TABLES

LIST OF FIGURES

SUMMARY

Command shaping creates reference commands that reduce residual vibrations in a flexible system. This thesis examines the use of command shaping for flexible system control in three industrial applications: cam-follower systems, sloshing liquids, and cherrypickers. One common type of command shaping is command smoothing which creates a smooth transition between setpoints. A specific type of command smoothing used in cam-follower systems is the polynomial profile. An alternative technique to reduce vibration in flexible systems is input shaping. In this thesis, input-shaped commands are compared to polynomial profiles for applications requiring both vibration suppression and fast motion. Simulation and experimental results show that input shaping is faster than polynomial profiles and provides a simple approach to suppressing residual vibration.

Secondly, significant experimental contributions have been made in the area of slosh control. The oscillation of liquids in a container can cause liquid spillage or can cause stability issues, especially in space vehicles. In the past, a number of control techniques have been proposed, but only a few recommend the use of input shaping. This thesis describes the use of command shaping to limit slosh. Results are supported by numerical and experimental testing. Input-shaped commands reduce residual slosh amplitude compared to unshaped commands and polynomial profiles. Input-shaped commands can also accommodate uncertainties and changes in the sloshing frequencies.

Lastly, a small-scale cherrypicker was constructed to study the use of input-shaping control on these types of aerial lifts. Cherrypickers have flexible dynamic effects that can cause dangerous and life-threatening situations. To study this class of machines and to provide future students an experimental testbed, several design criteria were established before construction began. The resulting machine achieved most design objectives, including a simple-to-use graphical user interface and accurate state measurements. Robust input-shaping controllers were implemented to limit endpoint vibration. The design of the cherrypicker is discussed and experimental results are reported.

CHAPTER I

INTRODUCTION

The motion of flexible systems is often limited by a desired positioning accuracy. For example, consider the crane model in Figure 1. As the crane trolley with mass *M* undergoes point-to-point motion, the payload with mass *m* suspended a length *L* below the trolley will respond with oscillations. For safe and efficient operation, the payload must be moved quickly and with minimal residual vibration. There are several ways to reduce residual vibration. One method is to adjust the mechanical design of the system. The system can be made more rigid, or damping can be added to the system. Another method is to implement feedback control, wherein sensors detect deviation from a desired setpoint and actuators correct the error.

A third method to limit residual vibrations in flexible systems is command shaping. One form of command shaping is smoothing the transition between setpoints [1, 6, 15, 19, 35, 44, 47, 65, 75, 76, 83]. Examples of smooth commands include polynomial profiles, s-curves, and trigonometric functions [32, 33, 50, 64]. There has been extensive work to design smooth command profiles to drive flexible systems and reduce residual vibration,

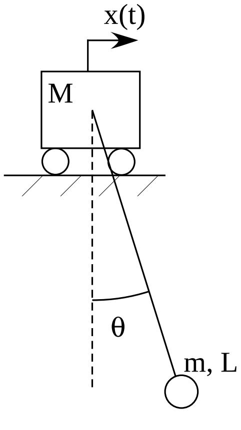

Figure 1. Crane Model

but inherent tradeoffs exist between vibration suppression, rise time, and ease of design [8].

Input shaping is a specific type of command shaping that reduces vibration in flexible systems. Using knowledge of the system natural frequency and damping ratio, input shaping provides a command design approach that results in a fast system response and minimal residual vibration [5,9,51,53,62]. As opposed to the low-pass filtering effect of most smooth commands, input shapers produce an effect similar to notch filters [52]. However, because input shapers do not have any pass-band constraints, they have much shorter durations than traditional notch filters. This characteristic leads to faster rise times [52,55].

This thesis compares polynomial profiles with input shaping in several industrial applications. Chapter 2 provides essential backround information through a review of polynomial profile design and input shaping. Chapter 3 compares polynomial profiles and input shaping with respect to rise time and vibration suppression characteristics. Input shaping is shown to be superior to polynomial profiles for vibration reduction, and this conclusion is verified in the subsequent chapters. Chapter 4 reports simulation and experimental results of slosh control using command shaping. Chapter 5 describes the design of a small-scale cherrypicker and experimental testing performed on the machine. This thesis then presents conclusions and suggests future work.

CHAPTER II

DESIGN PROCESS FOR POLYNOMIAL PROFILES AND INPUT-SHAPED COMMANDS

In addition to the crane model shown in Figure 1, the cam-follower in Figure 2 is another system with problematic flexible dynamics. The rotating cam surface profile inputs a desired displacement profile, $s(t)$, to the follower through some flexible connection, modeled by spring k_1. Additional flexibility and damping are modeled by spring k_2 and dashpot b. Ideally, the follower response, $y(t)$, tracks the desired displacement. However, such flexible systems often respond with undesirable vibrations [34, 82].

There are numerous cam profiles that limit residual vibrations [38, 50]. Some profiles use optimized trigonometric functions [17, 63, 74]. Other cam profiles aim to minimize the peak acceleration and jerk with cubic splines [80], or adjust coefficients of polynomials to achieve kinematic or residual vibration constraints [11, 81]. Polynomial profiles and other smooth profiles are also used as reference commands to drive automated machinery [20, 33, 64, 71, 73]. Polynomial profiles are one common class of cam profiles. This chapter gives an introduction to the design process for polynomial profiles and input-shaped commands.

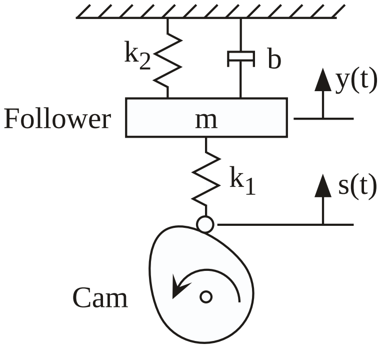

Figure 2. Cam-Follower System

2.1 Polynomial Profiles

A polynomial profile provides versatility and customization through the selection of boundary conditions for a desired motion. The general form of a polynomial profile is given by [38, 50]:

$$s(u) = C_0 + C_1 u + C_2 u^2 + \cdots + C_n u^n \tag{1}$$

The polynomial coefficients, C_n, are chosen to satisfy the boundary conditions and limit the dynamic response. The function $s(u)$ is the displacement of the profile where u is the normalized time such that $u = 0$ at the beginning of the motion and $u = 1$ at the end of the motion.

Two common polynomial profiles are the 3-4-5 and the 4-5-6-7, named for the order of the terms in the polynomial. The 3-4-5 polynomial provides continuity for the initial and final conditions of displacement, velocity $v(u)$, and acceleration $a(u)$:

$$\begin{gathered} s(0) = 0,\ v(0) = 0,\ a(0) = 0 \\ s(1) = h,\ v(1) = 0,\ a(1) = 0 \end{gathered} \tag{2}$$

where h is the magnitude of rise in the profile.

Solving for the coefficients of (1) using the boundary conditions in (2) gives the 3-4-5 polynomial profile:

$$s(u) = h(10u^3 - 15u^4 + 6u^5) \tag{3}$$

The 4-5-6-7 polynomial profile can be obtained by including additional constraints on the continuity of jerk $j(u)$, the third time-derivative of position:

$$\begin{gathered} j(0) = 0 \\ j(1) = 0 \end{gathered} \tag{4}$$

The 4-5-6-7 polynomial profile is:

$$s(u) = h(35u^4 - 84u^5 + 70u^6 - 20u^7) \tag{5}$$

The displacement, velocity, acceleration, and jerk of both polynomial profiles in the time domain are shown in Figure 3. It can be seen that each profile achieves a displacement

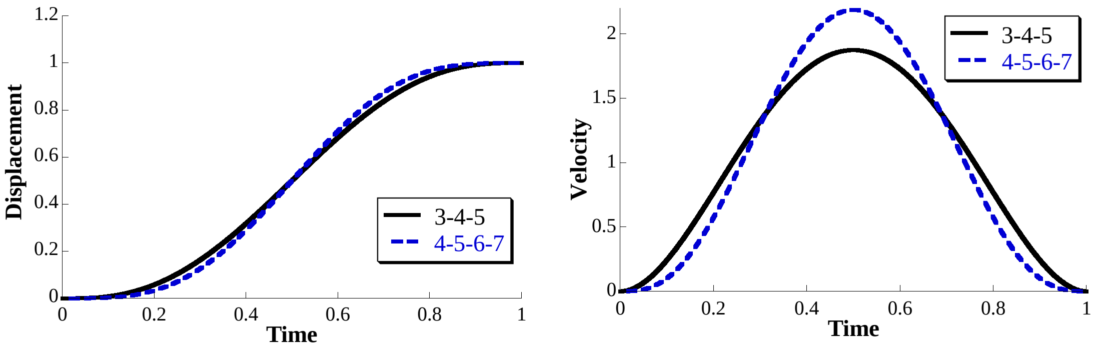

(a) Displacement (b) Velocity

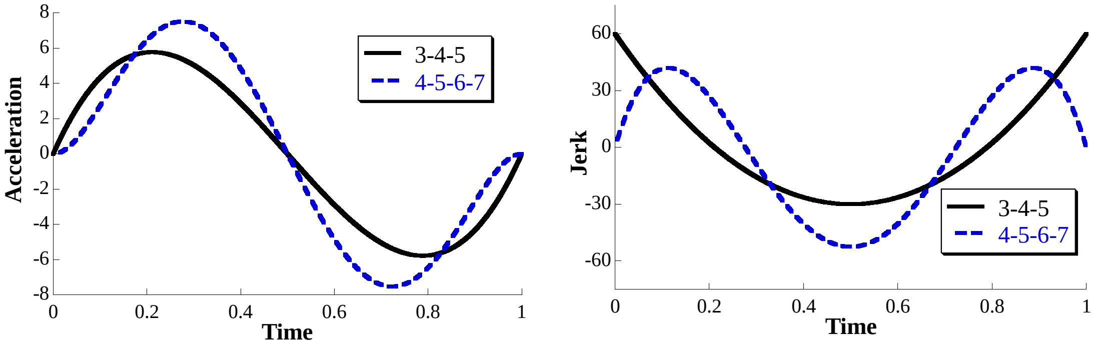

(c) Acceleration (d) Jerk

Figure 3. Polynomial Profile Motion Characteristics

from zero to one in 1.0 seconds. Because the 4-5-6-7 profile has an additional constraint, it has a higher peak velocity and acceleration. The jerk contiunity constraint of the 4-5-6-7 profile is also shown.

Rules of thumb can be used to select polynomial profiles, and additional constraints can be placed on transient characteristics to achieve a desired path [38, 50]. However, polynomial profiles provide no guarantee of satisfactory vibration reduction without an analysis of the full dynamic system. The method of input shaping discussed in the following section uses knowledge of the dynamic system during the design stage to produce minimal-vibration command profiles.

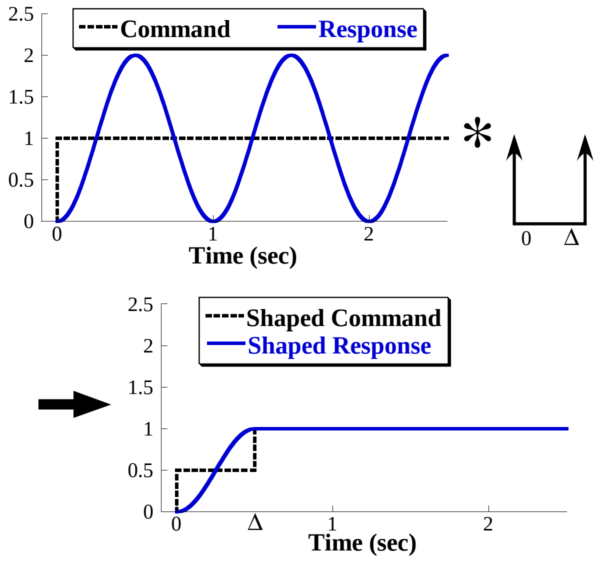

Figure 4. Input-Shaping Process

2.2 Input Shaping

The input-shaping process is illustrated in Figure 4. A baseline step command is convolved with an input shaper containing two positive impulses. The result of the convolution is the staircase command. Note that the baseline step command causes a residual vibration equal to the step amplitude; and the input-shaped command eliminates the residual vibration. Often, the baseline command used with input shaping is a step function because it yields the fastest rise time. However, the baseline command can also be a ramp, an S-curve, or any other command [14, 51, 53].

Input shapers are designed using knowledge of the system natural frequency, ω_n, and damping ratio, ζ. Constraint equations are used to determine n impulse times, t_i, and amplitudes, A_i. The first constraint is derived from the percentage residual vibration equation, given by [51]:

$$V(\omega_n,\zeta) = e^{-\zeta\omega_n t_n}\sqrt{(C(\omega_n,\zeta))^2 + (S(\omega_n,\zeta))^2} \tag{6}$$

where

$$C(\omega_n,\zeta) = \sum_{i=1}^{n} A_i e^{\zeta\omega_n t_i}\cos\left(\omega_n t_i\sqrt{1-\zeta^2}\right) \tag{7}$$

$$S(\omega_n,\zeta) = \sum_{i=1}^{n} A_i e^{\zeta \omega_n t_i} \sin\left(\omega_n t_i \sqrt{1-\zeta^2}\right) \tag{8}$$

Two additional constraints are placed on the impulse amplitudes. First, the sum of the amplitudes must equal one so that the input-shaped command reaches the setpoint:

$$\sum_{i=1}^{n} A_i = 1 \tag{9}$$

Second, the input shaper must be constrained to achievable commands. One method to attain realistic inputs is to set all amplitudes greater than zero:

$$A_i > 0, \quad i = 1,\ldots,n \tag{10}$$

Because there can be multiple solutions, the time of the last impulse is minimized to achieve the fastest command:

$$\min(t_n) \tag{11}$$

To eliminate residual vibration, V in (6) is set equal to zero. Therefore, both (7) and (8) must equal zero. These constraints give the amplitudes and time spacings of the impulses in the input shaper. For example, the shaper shown in Figure 4 is [54,62]:

$$\begin{bmatrix} t_i \\ A_i \end{bmatrix} = \begin{bmatrix} 0 & 0.5T_d \\ \frac{1}{1+K} & \frac{K}{1+K} \end{bmatrix} \tag{12}$$

where

$$K = e^{\left(\frac{-\zeta\omega_n}{\sqrt{1-\zeta^2}}\right)}, \tag{13}$$

and T_d is the damped period of vibration. The input shaper given in (12) produces zero vibration at the design frequency. As a result, it is called a Zero Vibration (ZV) shaper.

Another constraint can be added by taking the derivative of (6) with respect to ω and setting it equal to zero. This results in the more-robust Zero Vibration and Derivative (ZVD) input shaper. The time locations and amplitudes of a ZVD shaper are [51]:

$$\begin{bmatrix} t_i \\ A_i \end{bmatrix} = \begin{bmatrix} 0 & 0.5T_d & T_d \\ \frac{1}{1+2K+K^2} & \frac{2K}{1+2K+K^2} & \frac{K^2}{1+2K+K^2} \end{bmatrix} \tag{14}$$

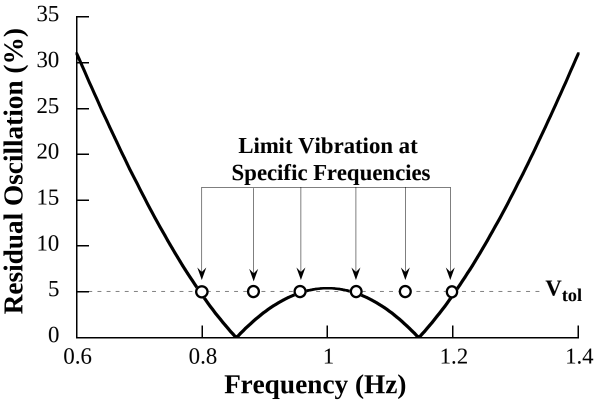

Figure 5. Specified Insensitivity (SI) Shaper Design Constraints

Even more robustness to changes in frequency can be obtained with an Extra-Insensitive (EI) input shaper [41,58]. This shaper is created by setting the percentage residual vibration constraint, V, in (6) to a non-zero tolerable value, V_{tol}. For an undamped system, the time locations and amplitudes of the EI shaper are given by:

$$\begin{bmatrix} t_i \\ A_i \end{bmatrix} = \begin{bmatrix} 0 & 0.5T_d & T_d \\ \frac{1+V_{tol}}{4} & \frac{1-V_{tol}}{2} & \frac{1+V_{tol}}{4} \end{bmatrix} \tag{15}$$

To eliminate multiple vibration modes, additional shapers or more complex shapers are required. A two-mode ZV-shaper (ZV2M) can be designed by simultaneously solving for the constraints of a two-mode system [27]. Specified Insensitivity (SI) shapers are generated by specifying a tolerable level of residual vibration over any desired range of frequencies [57,59]. One method for generating SI shapers uses multiple suppression constraints over the range of frequencies. At these distinct frequencies, residual vibration is constrained to below the tolerable percentage. For example, Figure 5 shows a case where residual vibrations are suppressed to below 5% of the vibrations caused an unshaped command over the range of 0.8 to 1.2 Hz.

However, it may be more meaningful to specify a tolerable *value* of vibration rather than specify a percentage of tolerable vibration [57]. For a value-based optimization, a new tolerable vibration constraint is written. For example, the sum of the residual vibration amplitude contributions of the first two modes, C_1 and C_2, should be less than a desired tolerable amplitude:

$$V_{tol} \geq V_{Amp} = C_1 + C_2 \tag{16}$$

From (16), a two-mode SI shaper (SI2M) can be developed.

CHAPTER III

COMPARISON OF POLYNOMIAL PROFILES AND INPUT SHAPING

This chapter provides a comprehensive comparison between polynomial profiles and input shaping and their use in flexible systems. First, it is shown that numerical methods are necessary to compare the two commands. Next, Section 3.2 reports the vibration-suppression properties of both types of commands with respect to rise time, robustness, and practical implementation considerations. Experimental results from a bridge crane are used to support the theoretical results.

3.1 *Frequency Analysis of Input Shapers and Polynomial Profiles*

Some smooth commands can be deconvolved into an initial command and an input shaper [56]. For example, a typical s-curve can be deconvolved into the initial command and input shaper shown in Figure 6. The shaper "embedded" in this s-curve has the impulse times and amplitudes of:

$$\begin{bmatrix} t_i \\ A_i \end{bmatrix} = \begin{bmatrix} 0 & \frac{R_c}{2} & R_c \\ 1 & -2 & 1 \end{bmatrix} \tag{17}$$

where, R_c is the risetime of the command.

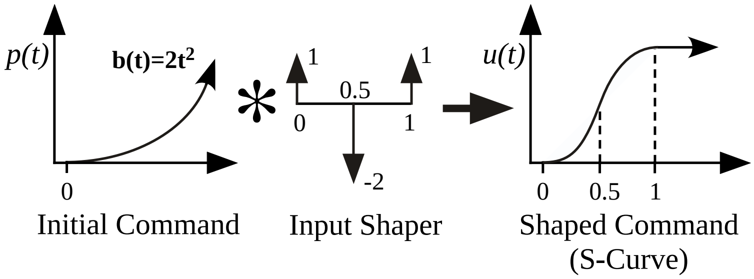

Figure 6. S-curve Convolution (From "Command generation for flexible systems by input shaping and command smoothing", Singhose, et al.)

The input shaper in (17) provides a useful tool to compare this command to input shaping. For example, the frequencies suppressed by the s-curve can be determined for a given rise time. Using such an analysis, it has been shown that the s-curve rise time must be four times longer than a ZV-shaped step command to suppress the same frequency. However, this decomposition cannot be done for all smooth commands. In this section, several common input shapers are shown to eliminate residual vibration at regularly-spaced frequencies. Then, it is shown that the 3-4-5 and 4-5-6-7 polynomial profiles do not eliminate residual vibration at regularly-spaced frequencies. Because polynomial profiles do not contain the periodic nature seen in input shapers, they do not contain an embedded input shaper. The results are generalized in the appendices to include all input shapers and all polynomial profiles.

3.1.1 Laplace Transform of Input Shapers

It has been shown that the amplitude-frequency response of the ZV shaper is a periodic function [42]. The analysis is extended here through the use of the Laplace transform. To find the frequencies where an input shaper yields zero residual vibration, its Laplace transform is set equal to zero [54]. The Laplace transform of a two-impulse shaper is:

$$A_1 + A_2 e^{-t_2 s} = 0 \tag{18}$$

For the ZV shaper, the relation between the two amplitudes is found from (12):

$$A_2 = A_1 e^{\frac{-\zeta\pi}{\sqrt{1-\zeta^2}}} \tag{19}$$

The time locations of the ZV impulses are also given in (12). Substituting the amplitude relation and time locations into (18) yields:

$$A_1 \left(1 + e^{\frac{-\zeta\pi}{\sqrt{1-\zeta^2}}} e^{-\frac{\pi}{\omega_d} s}\right) = 0 \tag{20}$$

This is further reduced to:

$$e^{-\frac{\pi}{\omega_d}(\zeta\omega_n + s)} = -1 \tag{21}$$

Substituting $s = \sigma + j\omega$ into (21) yields:

$$e^{-\frac{\pi}{\omega_d}(\zeta\omega_n+\sigma)} e^{-\frac{\pi}{\omega_d}j\omega} = -1 \tag{22}$$

In (22), there is a real and an imaginary exponential term. For the equation to hold true, the real term must equal 1, and the imaginary term must equal -1 [54]. This yields:

$$e^{-\frac{\pi}{\omega_d}(\zeta\omega_n+\sigma)} = 1 \tag{23}$$

$$e^{-\frac{\pi}{\omega_d}j\omega} = -1 \tag{24}$$

Therefore,

$$\sigma = -\zeta\omega_n \tag{25}$$

$$\cos\left(\frac{\pi\omega}{\omega_d}\right) - j\sin\left(\frac{\pi\omega}{\omega_d}\right) = -1 \tag{26}$$

The real cosine term in (26) must equal -1, and the imaginary sine term must equal zero.

$$\cos\left(\frac{\pi\omega}{\omega_d}\right) = -1 \tag{27}$$

$$\frac{\omega}{\omega_d} = 1, 3, 5, \ldots \tag{28}$$

and,

$$\sin\left(\frac{\pi\omega}{\omega_d}\right) = 0 \tag{29}$$

$$\frac{\omega}{\omega_d} = 1, 2, 3, \ldots \tag{30}$$

The solution of (28) contains *odd*, positive integers, and the solution of (30) contains positive integers. The overall solution is the intersection between the solution sets of (28) and (30), i.e. when ω/ω_d equals an odd, positive integer. Therefore, a ZV shaper eliminates residual vibration at regularly-spaced frequencies.

A similar procedure can be followed for the ZVD shaper. The corresponding real cosine and imaginary sine terms for the ZVD shaper are:

$$\cos\left(\frac{\pi\omega}{\omega_d}\right)\left(1 + \cos\left(\frac{\pi\omega}{\omega_d}\right)\right) = 0 \tag{31}$$

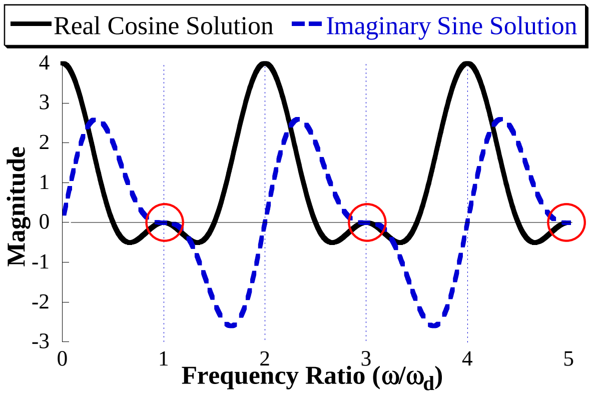

Figure 7. Overall ZVD Shaper Solution

and,

$$\sin\left(\frac{\pi\omega}{\omega_d}\right)\left(1+\cos\left(\frac{\pi\omega}{\omega_d}\right)\right)=0 \tag{32}$$

The overall solution for the ZVD shaper is found from the common terms of (31) and (32):

$$1+\cos\left(\frac{\pi\omega}{\omega_d}\right)=0 \tag{33}$$

$$\frac{\omega}{\omega_d}=1,3,5,\ldots \tag{34}$$

Similar to the ZV shaper, the ZVD shaper also eliminates residual vibration when the quantity ω/ω_d equals an odd, positive integer. To help visualize the solution, (31) and (32) are plotted in Figure 7. The solution is located at the points where the real cosine solution curve and the imaginary sine solution coincide on the zero axis. It is clear that each point, marked by a circle, occurs at regularly-spaced frequencies.

The EI shaper has a different solution due to the presence of the variable V_{tol}. The overall solution is:

$$\frac{\omega}{\omega_d}=\frac{1}{\pi}\cos^{-1}\left(\frac{V_{tol}-1}{V_{tol}+1}\right) \tag{35}$$

When V_{tol} equals zero, it is equivalent to the ZVD shaper, and so it eliminates residual vibration at odd, positive integers. At nonzero values of V_{tol}, residual vibration is eliminated at two points on either side of each odd, positive integer.

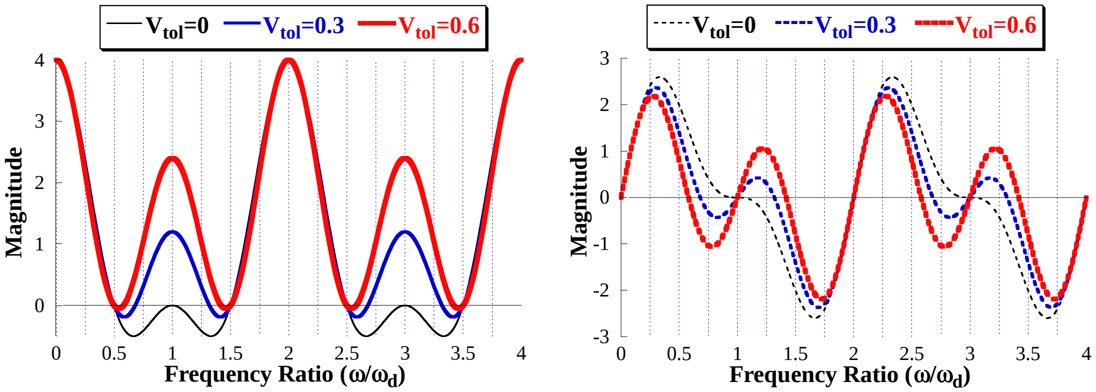

(a) Cosine Equation (b) Sine Equation

Figure 8. Solutions for the EI Shaper

To help visualize the solution, a family of curves is shown in Figure 8(a) for the cosine solution over a range of V_{tol} values. When V_{tol} equals zero, the cosine term is zero at frequency ratios of 1 and 3, and two symmetrical points about 1 and 3. For increasing values of V_{tol}, the zero-crossings move away from 1 and 3, but remain symmetrical about these points.

The same family of curves is shown for the sine solution in Figure 8(b). Similarly, as V_{tol} increases, the zero-crossings move away from frequency ratios of 1 and 3. The overall solution for the EI shaper is where the cosine and sine terms have mutual zeros. For $V_{tol} = 0.3$, these values occur at 1 ± 0.31, 3 ± 0.31, 5 ± 0.31, and so on. For $V_{tol} = 0.6$, these values occur at 1 ± 0.42, 3 ± 0.42, 5 ± 0.42, and so on. Like the previous shapers, the EI-shaper eliminates frequencies at regular intervals.

The Unity Magnitude Zero Vibration (UM-ZV) input shaper exhibits somewhat different behavior because it has a negative impulse [60]:

$$\begin{bmatrix} t_i \\ A_i \end{bmatrix} = \begin{bmatrix} 0 & \frac{T_d}{6} & \frac{T_d}{3} \\ 1 & -1 & 1 \end{bmatrix} \tag{36}$$

The zeros of the UM-ZV shaper are:

$$\frac{\omega}{\omega_d} = \frac{3}{\pi}\cos^{-1}\left(\frac{1}{2}\right) = 1, 5, 7, 11, 13, \ldots \tag{37}$$

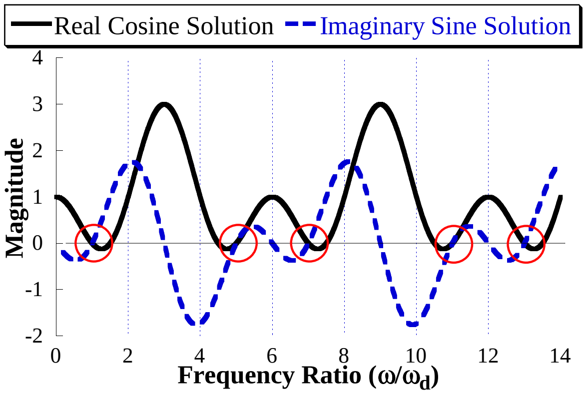

Figure 9. Overall UM-ZV Shaper Solution

For the UM-ZV shaper, the pattern is different than previously seen, but the zeros still repeat at a regular interval. The cosine and sine equations are plotted in Figure 9, and the locations of the overall solution frequency ratios are circled. These methods are generalized to include all input shapers in Appendix A.

Another way to demonstrate the periodic manner in which input shapers eliminate residual vibrations is with a vector diagram [58]. A vector diagram plots the impulses of an input shaper as vectors on a polar axis. Each vector begins at the origin. The length of a vector is equal to the amplitude of the corresponding impulse. The rotation angle of the vector is found by multiplying the system frequency, ω, by the time location of the impulse. If the impulse is negative, then the vector points toward the origin. The sum of the vectors determines the magnitude and phase of the residual vibration.

For example, consider the vector diagram of the ZV shaper shown on the left of Figure 10. For an undamped system at frequency ω, the first vector has a length of 0.5 and has an angle of zero. The second vector also has a length of 0.5 and is rotated by an angle $\theta = \omega t_2$. If the ZV shaper is designed perfectly ($t_2 = \frac{\pi}{\omega}$), then the second vector will be exactly opposite of the first vector ($\theta = \omega\frac{\pi}{\omega} = \pi$). The two vectors sum to zero, demonstrating that the ZV shaper eliminates residual vibration. Now consider a system where ω is three times the original value, as shown on the right of Figure 10. With the same ZV shaper, the second vector now has an angle of 3π and appears in the same location. The sum of

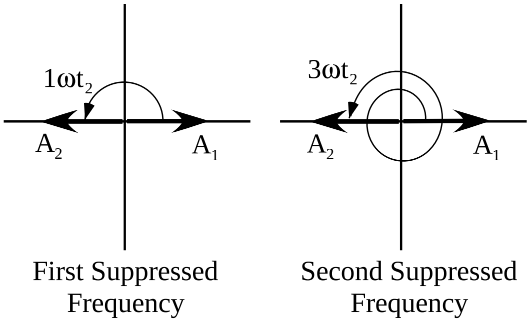

Figure 10. Vector Diagrams for a ZV shaper

the vectors for this new system is also zero. This vector diagram analysis shows that if the first design frequency is multiplied by any odd, positive integer, then the ZV shaper will eliminate residual vibrations.

Similar vector diagrams can be generated for the ZVD and EI shapers to show that they also eliminate residual vibrations at or near every odd, positive integer multiple of the first frequency.

A vector diagram of the first suppressed frequency of the UM-ZV shaper is shown in the top left of Figure 11. The three vectors clearly add to zero. In the top right, the system frequency is increased by a factor of five. The vectors are mirrored across the horizontal axis and still add to zero. The three vectors return to their original locations when ω is seven times the original value, shown in the bottom of Figure 11. This pattern continues, in accordance with (37).

3.1.2 Continuous Fourier Transform of Polynomial Profiles

The 3-4-5 polynomial profile can be converted to the frequency domain using the continuous Fourier transform (CFT). Over the interval $-\infty$ to ∞, the polynomial profile is piecewise. For a 3-4-5 polynomial with a rise of one and a rise time of one, the piecewise

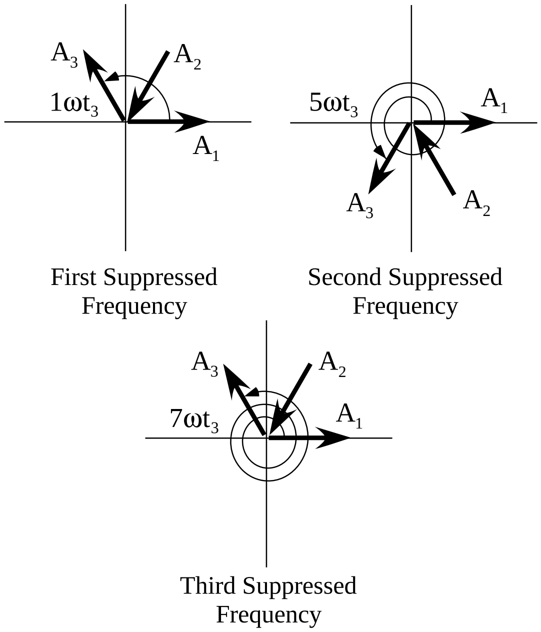

First Suppressed Frequency

Second Suppressed Frequency

Third Suppressed Frequency

Figure 11. Vector Diagrams for a UM-ZV shaper

equation is given by:

$$x(t) = \begin{cases} 0 & t < 0 \\ 10t^3 - 15t^4 + 6t^5 & 0 \le t \le 1 \\ 1 & 1 < t \end{cases} \tag{38}$$

The magnitude of the CFT gives the frequency content of the command. For the 3-4-5 polynomial, this is:

$$\begin{aligned} |X(j\omega)| = \frac{60}{\omega^6}\big[&-288\cos(\omega) + 120\omega^2\cos(\omega) \\ &-2\omega^4\cos(\omega) - 288\omega\sin(\omega) \\ &+24\omega^3\sin(\omega) + 288 + 24\omega^2 + 2\omega^4\big]^{1/2} \end{aligned} \tag{39}$$

The plot of this function in Figure 12 shows the frequency content over a range of frequencies. At certain frequencies, the magnitude is zero. These are the frequencies where the 3-4-5 profile completely eliminates residual vibration. The location of these zeros is particularly important. Note that the frequency is not normalized because this polynomial command was not designed for a specific frequency.

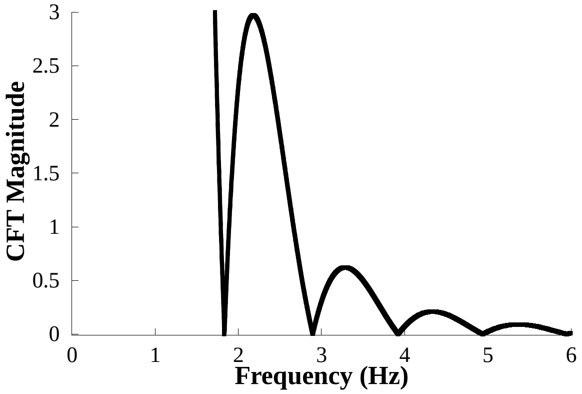

Figure 12. Magnitude of 3-4-5 Polynomial CFT

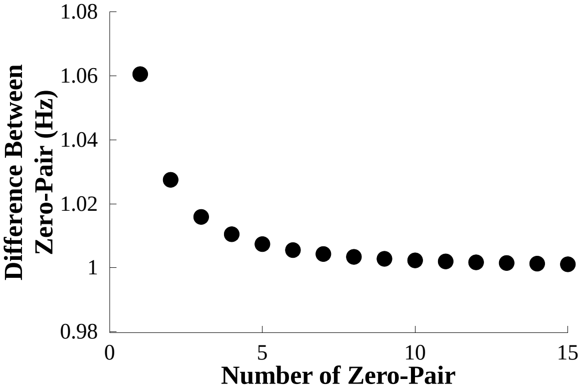

Figure 13. Difference Between Sequential Zeros of Figure 12

The first fifteen zeros were numerically determined, and the frequency difference between sequential zeros (zero-pairs) is shown in Figure 13. The difference between zero-pairs is not constant; but as the zero-pair approaches infinity, the difference approaches 1 Hz. This is a result of the last two terms in (39). From this equation, it can be noted that the 3-4-5 polynomial profile does not eliminate vibration at regularly-spaced frequencies.

The magnitude of the CFT of the 4-5-6-7 polynomial profile is:

$$\begin{aligned} |X(j\omega)| = \frac{840}{\omega^8}\big[&-15840\omega\sin\omega+3144\omega^3\sin\omega \\ &-48\omega^5\sin\omega-2880\cos\omega+10368\omega^2\cos\omega \\ &-528\omega^4\cos\omega+2\omega^6\cos\omega+14544 \\ &+4032\omega^2+48\omega^4+2\omega^6\big]^{1/2} \end{aligned} \tag{40}$$

The last three terms in (40) similarly show that the 4-5-6-7 polynomial profile does not eliminate vibration at regularly-spaced frequencies. For a generalization that extends to all polynomial profiles, refer to Appendix B.

In this section, common input shapers were shown to eliminate residual vibration at periodically-spaced frequencies, and this conclusion was extended to include all input shapers in Appendix A. It was also shown that the 3-4-5 and 4-5-6-7 polynomial profiles do not eliminate residual vibration in a periodic manner, and this conclusion was extended to include all polynomial profiles in Appendix B. If some command can be decomposed into a baseline command convolved with an input shaper, then the frequency domain of the command must contain periodically-spaced zeros. Because polynomial profiles do not contain periodically-spaced zeros in the frequency domain, there cannot be an input shaper embedded in polynomial profiles.

3.2 Comparison of Polynomial Profiles and Input-Shaped Commands

Given that both polynomial profiles and input-shaped commands are used to drive flexible systems, it is important to understand their relative strengths and weaknesses. First, typical responses of polynomial profiles and input-shaped commands are shown. Then, comparisons are made with respect to rise time and robustness. Practical implementation considerations are also discussed.

3.2.1 Polynomial Profile Command Responses

Consider the single degree-of-freedom cam-follower system in Figure 2 with a natural frequency of 1 Hz and no damping. The follower response of this system to three different 3-4-5 polynomial profiles with different rise times is shown in Figure 14. The first rise time is equal to half of the period of oscillation (0.5 s); the second rise time is equal to one period of oscillation (1.0 s); and the last rise time produces residual vibration that is 5% of the move distance (1.68 s). Corresponding results for the 4-5-6-7 polynomial profile are shown in Figure 15.

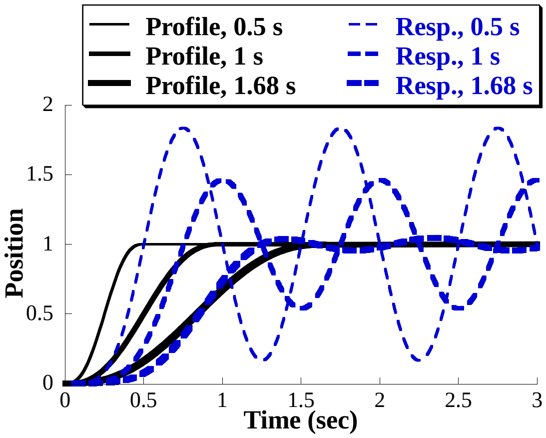

Figure 14. 3-4-5 Polynomial Profile Responses

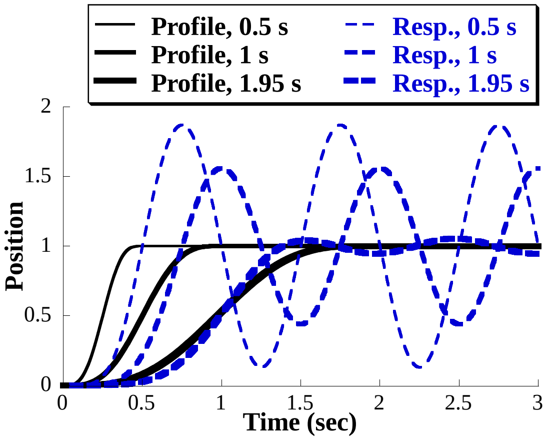

Figure 15. 4-5-6-7 Polynomial Profile Responses

The half-period 3-4-5 and 4-5-6-7 profiles induce residual vibration amplitudes greater than 80% of the move distance. With a rise time equal to one period, the residual vibration amplitudes are reduced to 46% and 56%, respectively. To achieve residual vibrations of 5%, the polynomial profiles require rise times of 1.68 and 1.95 seconds, respectively. If the residual vibration amplitude must be suppressed even further, then the rise times of the polynomial profiles must increase.

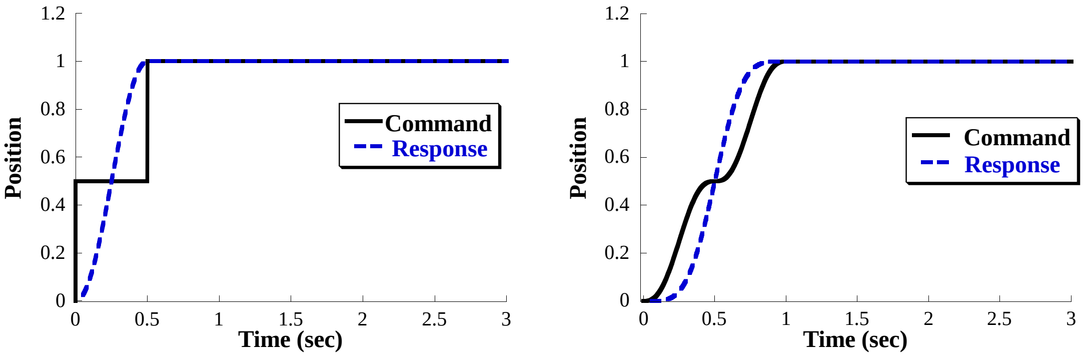

(a) ZV-Shaped Step Command (b) ZV-Shaped Smooth Command

Figure 16. Response of a One-Mode System (1 Hz) to ZV-Shaped Commands

3.2.2 Input-Shaped Command Responses

Two ZV-shaped commands were designed for the single degree-of-freedom, 1-Hz undamped system. The first command uses a baseline step command. This results in the fastest-possible ZV-shaped command with a rise time of 0.5 seconds. The second command is a shaped smooth command [5]. Here, the baseline command is a 3-4-5 polynomial command with a rise time of 0.5 seconds, which produces a shaped command with a rise time of 1 second. This shaped command will be abbreviated as “ZV-shaped smooth”. It is slower than the shaped step command, but provides a low-pass filtering effect similar to the polynomial profiles. Refer to [56] for guidelines regarding the use of smooth baseline commands with input shapers. These two ZV-shaped commands and the follower responses are shown in Figures 16(a) and 16(b). Both commands eliminate residual vibration for this system.

The benefit of the low-pass filtering effect of the ZV-shaped smooth command can be seen in a system with additional modes of vibration. The responses of a two-mode system with frequencies of 1 Hz and 3.5 Hz are shown in Figures 17(a) and 17(b). It can be seen that the ZV-shaped step command eliminates the first vibratory mode, but there is noticeable residual vibration at the higher frequency. However, the low-pass filtering effect of the ZV-shaped smooth command eliminates most of the residual vibration at the higher

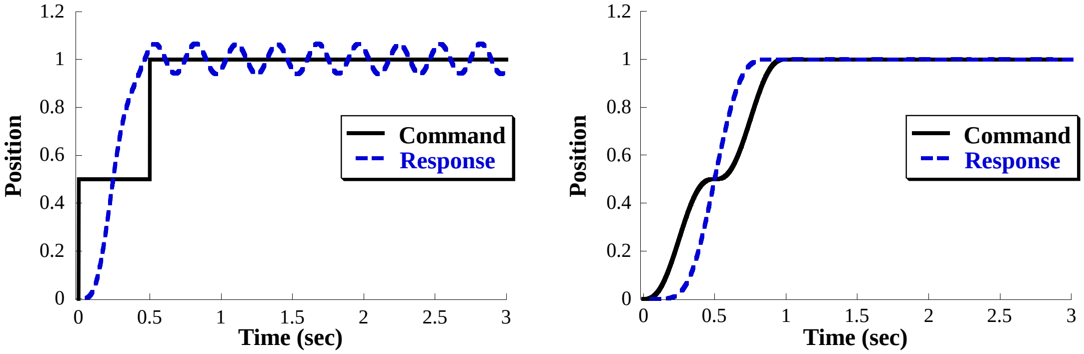

(a) ZV-Shaped Step Command

(b) ZV-Shaped Smooth Command

Figure 17. Response of a Two-Mode System (1 Hz and 3.5 Hz) to ZV-Shaped Commands

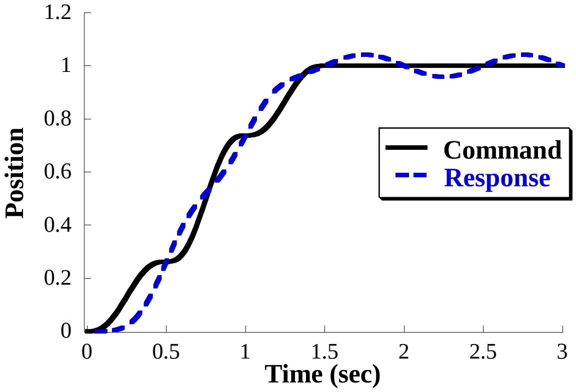

Figure 18. Response of a One-Mode System (1 Hz) to an EI-Shaped Command

frequency.

An EI-shaped command was also created using the same baseline command as the ZV-shaped smooth command and with a tolerable residual vibration, V_{tol}, of 5%. The one-mode system response is shown in Figure 18. Because the system operates exactly at the design frequency, there is 5% residual vibration. However, this shaped command is very robust to deviations in system frequency, and will be discussed further in Section 3.2.3.

3.2.3 Rise Time and Robustness

It is often desired to move a system rapidly without exciting resonances. Table 1 compares the rise times, R, of polynomial profiles to input-shaped step commands. The values are

Table 1. Comparison of Rise Times to Achieve 5% Residual Vibration

3-4-5 Profile	4-5-6-7 Profile
$R_{ZV} = 0.29\ R_{3\text{-}4\text{-}5}$	$R_{ZV} = 0.24\ R_{4\text{-}5\text{-}6\text{-}7}$
$R_{ZVD} = 0.50\ R_{3\text{-}4\text{-}5}$	$R_{ZVD} = 0.43\ R_{4\text{-}5\text{-}6\text{-}7}$
$R_{EI\text{-}5\%} = 0.47\ R_{3\text{-}4\text{-}5}$	$R_{EI\text{-}5\%} = 0.39\ R_{4\text{-}5\text{-}6\text{-}7}$
$R_{UMZV} = 0.19\ R_{3\text{-}4\text{-}5}$	$R_{UMZV} = 0.16\ R_{4\text{-}5\text{-}6\text{-}7}$

for the fastest commands that achieve 5% residual vibration in a one-mode system. For example, to suppress vibration in a given system, the rise time of a ZV-shaped step command is only 29% of the rise time of a 3-4-5 polynomial profile. For an EI-shaped command designed with 5% tolerable vibration, the rise time is 47% of the rise time for a 3-4-5 polynomial profile. Input-shaped commands show an even greater benefit over the 4-5-6-7 polynomial profile. The fastest command is the UMZV-shaped command, which has a rise time of only 16% of the 4-5-6-7 polynomial profile. It should be noted that convolving a different baseline command with the input shaper may result in different rise times.

Robustness is an important design consideration to accommodate modeling errors or changes in the system. Figure 19 shows the percent residual vibration amplitude resulting from two ZV-shaped commands and one EI-shaped command designed for a system frequency of 1 Hz. Here, 100% residual vibration corresponds to the vibration induced by a step command, and robustness is defined as the frequency range over which a command induces less than 5% vibration. At the design frequency (1 Hz), the two ZV-shaped commands eliminate residual vibration, and the EI-shaped command reduces residual vibration to 5%. However, the EI-shaped command is over six times as robust as the ZV-shaped commands [58]. At higher frequencies, the ZV-shaped step command eliminates vibration at odd multiples of the design frequency. The smooth baseline command of the ZV-shaped and EI-shaped smooth commands provides a low-pass filtering effect. The residual vibration induced by these commands is reduced to 5% at all frequencies greater than 2.8 Hz and 2.6 Hz, respectively.

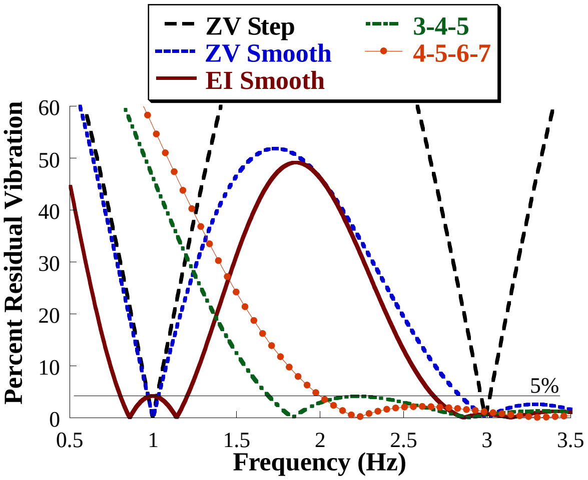

Figure 19. Residual Vibration Amplitudes

Figure 19 also shows the vibration induced by two polynomial profiles. The polynomial commands have rise times equal to the ZV-shaped smooth command. The 3-4-5 and 4-5-6-7 polynomial profiles induce over 45% residual vibration at 1 Hz. The 3-4-5 and 4-5-6-7 profiles do reduce residual vibration to 5% at frequencies greater than 1.7 Hz and 2.0 Hz, respectively.

3.2.4 Practical Considerations

One weakness of polynomial profiles used for reference motion commands is that they cannot be generated on-the-fly. When polynomial profiles are used to generate trajectory commands, a path is generated according to desired boundary conditions. There are two limitations to this requirement. First, a move command must reach its final state before a successive move command can begin. Second, if a move command is interrupted during the move, then the low-pass filtering effect is eliminated. Input shaping overcomes these limitations by convolving an input with an input shaper in real-time. By this method, any desired movement results in reduced residual vibration. Move commands can be generated on-the-fly without regard for previous move commands and without the need for the system to finish any current motion it might be executing.

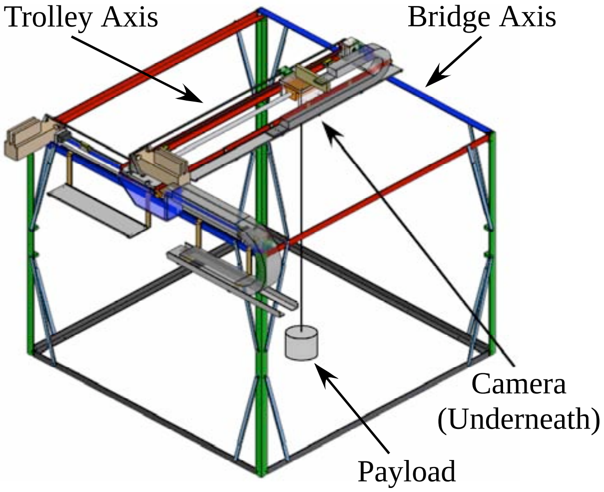

Figure 20. Portable Bridge Crane

3.3 Experimental Results

Testing was conducted on the portable bridge crane sketched in Figure 20. The bridge and trolley axes are driven by servomotors, and an overhead camera provides precise, real-time measurements of the payload location [31]. Using a payload suspended 70 cm below the trolley ($f = 0.59$ Hz), move commands were generated using the 3-4-5 and the 4-5-6-7 polynomial profiles to achieve a 20 cm move distance. ZV-shaped and EI-shaped smooth commands were designed to eliminate vibrations for a 0.59 Hz system. The risetimes of the ZV-shaped and EI-shaped commands were 1.7 and 2.5 sec, respectively. Because these commands contain a smooth profile as the basline command, their risetimes are greater than that of a shaped-step commands.

The effect of increasing the rise time of polynomial profiles on residual vibration was investigated. For each test, the rise time was increased from 1.7 seconds until 5% residual vibration was achieved. The results are shown in Figure 21. The 3-4-5 and 4-5-6-7 polynomial profiles resulted in 44% and 55% residual vibration, respectively, when the rise time was set equal to the ZV-shaped command (1.7 s). The polynomial profiles resulted in 10% and 21% residual vibration when the rise time was set equal to the EI-shaped command (2.5 s). In order to achieve 5% residual vibration, the 3-4-5 profile required a rise time of

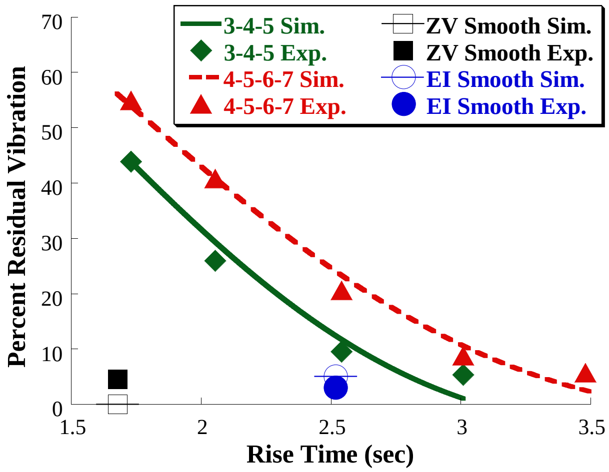

Figure 21. Experimental Testing of Rise Time

3.0 seconds, and the 4-5-6-7 profile required a rise time of 3.3 seconds. On the other hand, both shaped commands resulted in residual vibration amplitudes of less than 5%.

The robustness of the commands was studied by testing them over a range of system frequencies by changing the height of the suspended payload. The same ZV- and EI-shaped commands were used, and the polynomial profiles had rise times equal to the rise time of the ZV-shaped smooth command (1.7 sec). The results are shown in Figure 22. The ZV-shaped command resulted in less than 5% residual vibration at the design point of 0.59 Hz. The residual vibration increased as the system deviated from the design point. The EI-shaped command was more robust; it limited residual vibration to less than 5% between 0.49 Hz and 0.72 Hz. The polynomial profiles with the given rise time could not reduce residual vibration to 5% in the workspace that was measurable by the data acquisition camera. It is interesting to note that the polynomial profiles produced larger-than-expected vibrations. This was a result of stiction in the motors that prevented small velocity changes. Stiction did not induce greater vibrations in the input-shaped cases because it was a component of the baseline command and not the input shaper. These experimental results confirm the results shown in Figure 19.

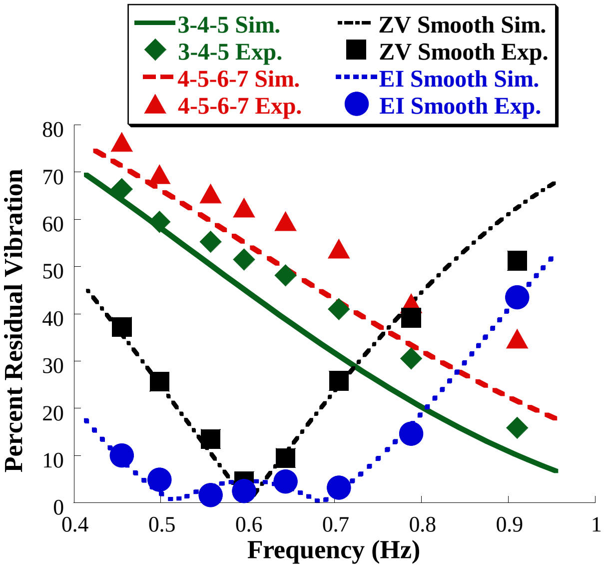

Figure 22. Experimental Testing of Robustness

CHAPTER IV

SLOSH CONTROL

4.1 Introduction

Slosh is the oscillation of liquid inside a container. There are many cases where sloshing is undesired. In the packaging and metal industries, excessive slosh can spill liquids or molten metal [67]. Sloshing of fuel and other liquids in vehicles can result in unwanted dynamics and dangerous rollovers [4]. This is especially true for space vehicles where excessive slosh can cause instability [43].

There has been significant research to characterize and control slosh. A main thrust of research was driven by NASA. This work covered the governing equations, experimental results for a variety of container shapes, and the modeling of slosh [3,13,28,49]. There have been more recent studies of slosh in space vehicles which investigated liquid type [24, 25], container shape [69, 70], and spacecraft motion [26, 46].

In order to suppress slosh, a variety of methods have been proposed, simulated, and tested. Some techniques are passive [36], or rely on actuators near the liquid surface for slosh suppression [23, 72]. However, it is often not practical to place actuators in or near the liquid. The majority of proposed techniques use the container motion as the control input in a feedback loop. Examples of these include: sliding mode control [7, 30]; H_∞ control [67, 79]; PID control [61]; a hybrid shape approach [29, 37, 77, 78]; and iterative learning control [21]. Some control schemes filter the input to create a prescribed motion that results in minimal residual oscillation [10,16]. Several experimental test rigs have been constructed [2, 3, 16, 18, 22, 68].

There have been several implementations of input shaping as a means to control slosh [2, 16, 22, 45, 66, 68]. However, no reports have shown experimental verification of input

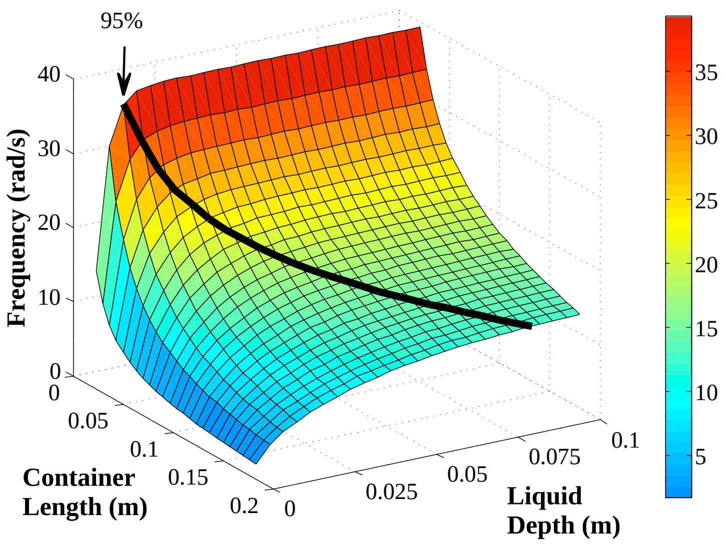

Figure 23. Slosh Frequency of Liquid Surface

shapers that are robust to parameter variation. This chapter reports simulated and experimental evaluation of robust input shaping for slosh suppression.

4.2 System Modeling

4.2.1 Slosh

The natural frequency of the i^{th} mode of a liquid surface in a rectangular container can be described by [3]:

$$\omega_{n_i}^2 = (2i-1)\frac{g\pi}{a}\tanh\left((2i-1)\frac{h\pi}{a}\right) \tag{41}$$

where g is the gravitational acceleration, a is the container length in the direction of wave motion, and h is the liquid depth. Several assumptions are utilized to arrimve at this simplified equation, including zero liquid viscosity. Note that the container width is not an influence on the frequencies. Experimental testing has shown that (41) often predicts the frequency with less than 5% error [39].

A three dimensional surface plot of the fundamental slosh frequency versus container length and liquid depth is shown in Figure 23. Increasing the container length results in a lower slosh frequency because the wave must travel further before being reflected. As the liquid depth increases, the hyperbolic tangent term approaches unity and the frequency approaches a theoretical limit. As a result, the slosh frequency changes very little after a critical depth. The line superimposed on Figure 23 shows the liquid depths at which the slosh frequency reaches 95% of its maximum value. This line corresponds to liquid depths that are approximately half of the container length.

Analytical expressions have also been developed for the damping ratio, showing it to be approximately 0.01 for water. The analytical expression for the damping ratio is a function of an experimentally-found constant, the Galilei number, and container geometry. However, it can have up to 25% error [3,39]. Given this uncertainty, the damping ratios for the tests reported here were determined experimentally.

4.2.2 Dynamic System Model

A container with sloshing liquid can be approximated by the model shown in Figure 24. The container motion $y(t)$ induces a damped vibratory response, $x_i(t)$, in the i^{th} mode. This is a linearized form of the commonly-used pendulum model of slosh. Each additional vibratory mode of slosh is modeled by an additional mass-spring-damper system. The first two modes of slosh are modeled in Figure 24. The combined mass of the container and stationary liquid is m_0, and the dimensions a and h used in (41) are also illustrated. The equation of motion for the i^{th} mode of the system is:

$$\ddot{x}_i + 2\zeta_i \omega_{n_i} \dot{x}_i + \omega_{n_i}^2 x = 2\zeta_i \omega_{n_i} \dot{y} + \omega_{n_i}^2 y \tag{42}$$

where ω_{n_i} is given in (41), and ζ_i is determined experimentally.

Converting (42) to the s-domain yields:

$$X(s) = \left(\frac{2\zeta_i \omega_{n_i} s + \omega_{n_i}^2}{s^2 + 2\zeta_i \omega_{n_i} s + \omega_{n_i}^2} \right) Y(s) \tag{43}$$

The motion of the liquid surface, $\delta(t,w)$, is a function of time and the measurement location w. The rightmost edge of the container, measurement location a, is of particular

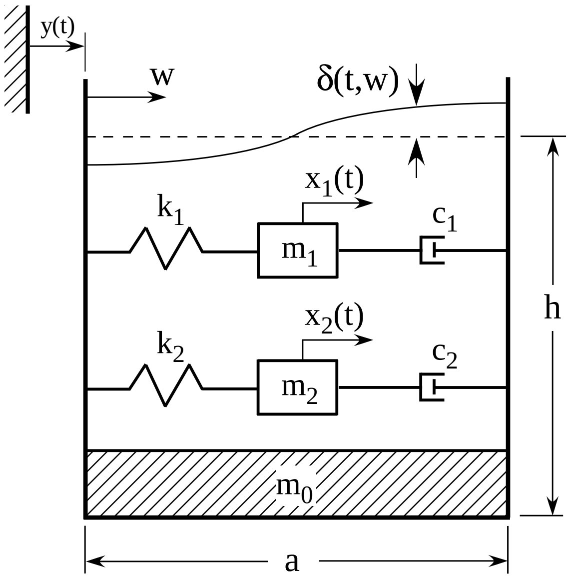

Figure 24. Slosh Model

interest because it is the anti-node of the mode shapes and where spillage occurs [3]. The motion at location a is the sum of the relative motions between x_i and y:

$$\delta(t,a) = \sum_{i=1}^{n} x_i(t) - y(t) \tag{44}$$

The motion of the liquid surface at location a caused by a step in velocity of the container is:

$$\delta(t,a) = |\dot{Y}| \sum_{i=1}^{n} \left(\frac{1}{\omega_{d_i}}\right) e^{-\zeta_i \omega_{n_i} t} \sin \omega_{d_i} t \tag{45}$$

where $|\dot{Y}|$ is the velocity amplitude and the damped natural frequency is:

$$\omega_{d_i} = \omega_{n_i} \sqrt{1-\zeta_i^2} \tag{46}$$

In order to design a value-based input shaper, the amplitude contributions of the first two modes can be found in (45). As described in Chapter 2, the sum of these contributions should be less than a tolerable amplitude:

$$V_{tol} \geq V_{Amp} = |\dot{Y}| \left(\frac{1}{\omega_{d_1}} + \frac{1}{\omega_{d_2}}\right) \tag{47}$$

From (47), a two-mode SI shaper (SI2M) can be designed.

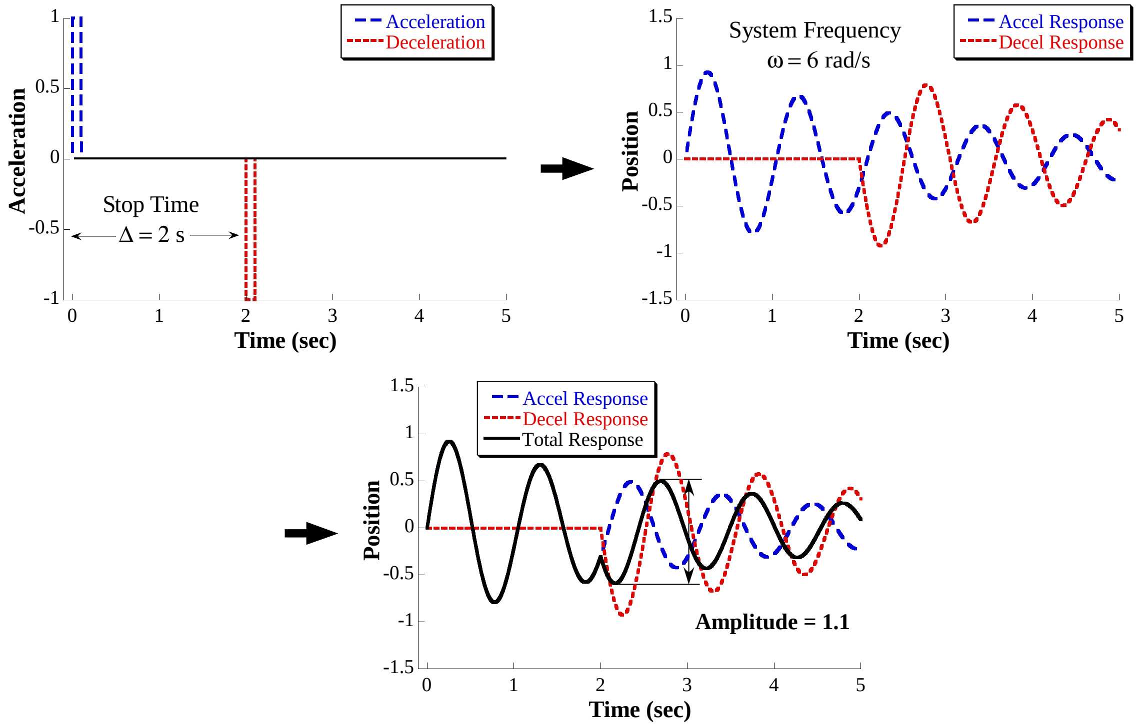

Figure 25. Wave Interference for 2-Second Move, ($\omega = 6$ rad/s)

4.2.3 Wave Interference

When considering point-to-point motions, it is important to understand how vibrations induced by the ‘go’ command may interfere with vibrations induced by the ‘stop’ command. For example, an acceleration pulse and a deceleration pulse (delayed by 2 seconds) are shown in the top left of Figure 25. The acceleration pulse would cause a one-mode system ($\omega = 6$ rad/s) to respond with the oscillations shown by the dashed line in the top right of Figure 25, and the deceleration pulse would induce the oscillations shown by the dotted line. The total linear system response is the sum of these two waves, and is shown in the bottom of Figure 25. In this case, the residual vibration amplitude is 1.1.

If the move time changes, then the residual vibration amplitude may differ, despite the system receiving the same acceleration and deceleration pulses. In Figure 26, the deceleration pulse occurs at 2.5 seconds. The oscillations induced by each pulse are shown, and the total response has a residual vibration amplitude of 2.3. If the system frequency

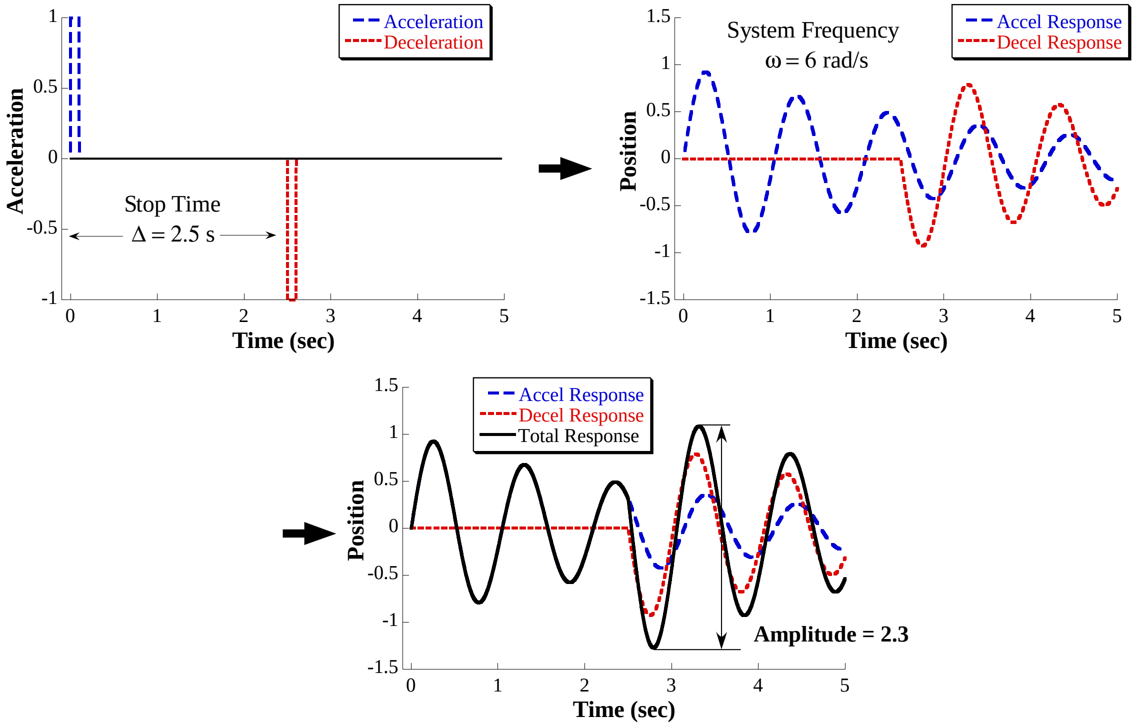

Figure 26. Wave Interference for 2.5-Second Move ($\omega = 6$ rad/s)

changes, then a different amount of residual vibration will be generated, despite using the same acceleration and deceleration. In Figure 27, the deceleration impulse is again set at 2 seconds, but the system frequency has changed from 6 rad/s to 5 rad/s. With this lower frequency, the total system response has a residual vibration amplitude of 2.7, rather than the 1.1 vibration amplitude that occurs with a frequency of 6 rad/s.

4.3 Testing Apparatus

For experimental testing, the container and camera in Figure 28 were mounted to an XY gantry. The gantry was driven by servomotors and controlled by a programmable logic controller [31]. The camera recorded the slosh inside the container. Parameters of the experimental setup are given in Table 2.

Each video frame from the experimental trials was extracted from the video, as shown in Figure 29(a). The image was then thresholded, as shown in Figure 29(b). The surface of the water was located from the boundary between whte and black, and is shown in

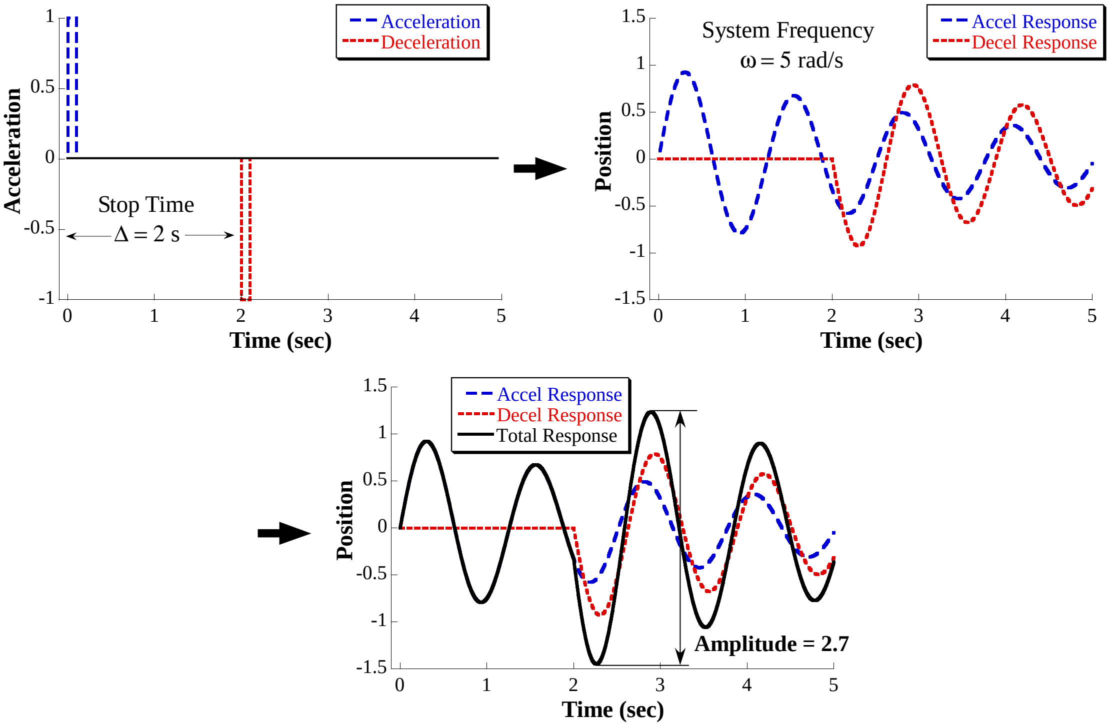

Figure 27. Wave Interference for 2-Second Move ($\omega = 5$ rad/s)

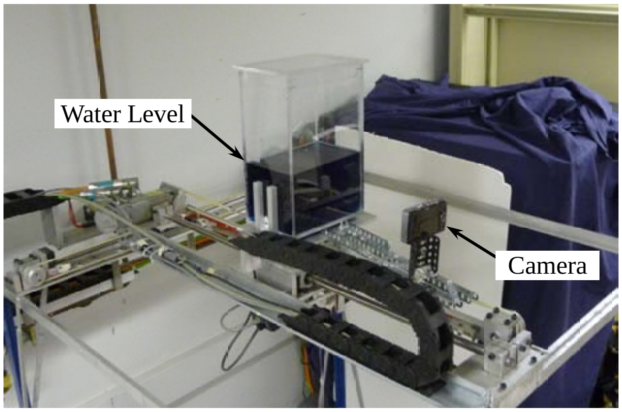

Figure 28. Testing Apparatus

Table 2. Experimental Parameters

Container length (m)	0.18
Move distance (m)	0.36
Peak velocity (m/s)	0.18
Acceleration (m/s^2)	1.5
Camera frame rate (Hz)	30
Camera resolution (mm)	0.35

(a) Image Frame

(b) Thresholded Image

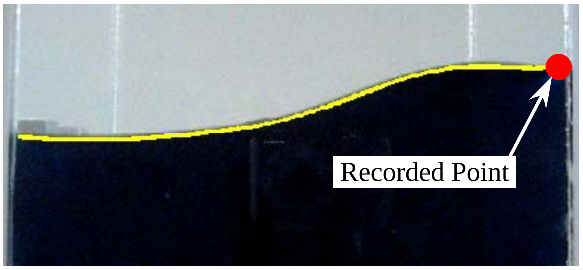

(c) Boundary and Recorded Point

Figure 29. Image Processing

Figure 29(c). To measure slosh, the displacement of the rightmost point on the surface was recorded for each image. This point is denoted by the circle in Figure 29(c). The damping ratios of the first two modes were experimentally found to be 0.010 and 0.015 using the logarithmic decrement.

4.4 Command Design

When designing commands for a system with sloshing dynamics, it is important to understand which modes of oscillation are important and how the sloshing frequencies will change. Some applications only consider the first mode of slosh [26], while other applications may require consideration of the second mode. In addition, the frequencies may change significantly due to varying liquid depth, or the frequencies may remain relatively constant during operation.

Four input shapers were designed to accommodate each scenario: one- or two-mode suppression, and robust or not robust to frequency changes. A single-mode, non-robust ZV shaper was designed for a frequency of 12.5 rad/s (a liquid depth of 8.7 cm). A single-mode EI shaper was designed for a frequency of 10.9 rad/s (a liquid depth of 4.9 cm) and with a 5% tolerable vibration. A two-mode ZV shaper (ZV2M) was designed for frequencies of 12.5 rad/s (a liquid depth of 8.7 cm at the first mode), and 22.1 rad/s (3.5 cm at the second mode). A two-mode value-based SI shaper (SI2M) was designed using (47) to suppress slosh for frequencies between 9.1 rad/s and 13.1 rad/s (liquid depths $>$ 3 cm for the first mode) and 21.7 rad/s and 22.7 rad/s (liquid depths $>$ 3 cm for the second mode) with a maximum residual vibration amplitude of 10 mm. For simulations and testing, these input shapers were convolved with a baseline trapezoidal velocity command. The impulse times and amplitudes of the four shapers are given in Table 3.

Two polynomial profiles were also designed to move the liquid container. The 3-4-5 and 4-5-6-7 polynomial profiles given in (3) and (5) were designed with rise times equal to the SI2M shaper duration (0.590 s).

Figure 30 shows a plot of the expected percent residual vibration amplitude resulting from the input shapers as a function of slosh frequency. As a general rule, 5% residual vibration is considered acceptable here. For liquid depths $>$ 3 cm, the first mode frequencies for the container range from 9.1 - 13.1 rad/s. The liquid depth of 3 cm was chosen because spillage was very unlikely to occur at this depth for the given container. Around the region

Table 3. Shaper Impulse Amplitudes and Times

ZV	t_i	0	0.247		
	A_i	0.51	0.49		
EI	t_i	0	0.288	0.576	
	A_i	0.27	0.48	0.25	
ZV2M	t_i	0	0.183	0.363	
	A_i	0.32	0.39	0.29	
SI2M	t_i	0	0.207	0.385	0.590
	A_i	0.22	0.29	0.29	0.20

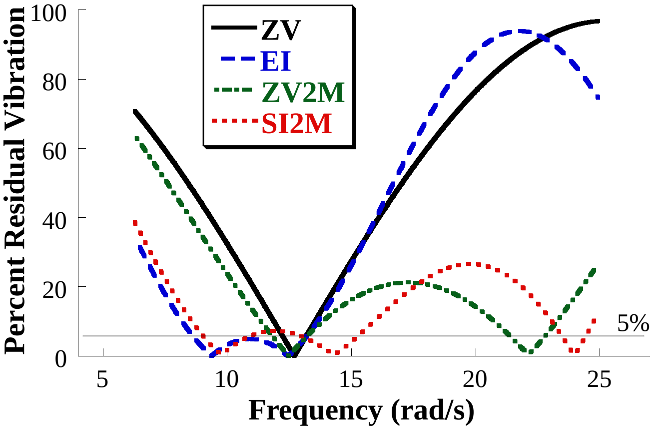

Figure 30. Input Shaper sensitivity

of the first mode, the ZV and ZV2M shapers suppress a relatively small range of frequencies below 5%. The EI and SI2M shapers suppress a much wider range of frequencies around the first mode.

The second mode frequencies range from 21.7 - 22.7 rad/s for liquid depths $>$ 3 cm. In this range, the ZV and EI shapers clearly do not perform well. However, the ZV2M shaper has a region of 5% suppression at the higher mode. The percent residual vibration of the SI2M shaper is slightly greater than the ZV2M shaper at the higher mode because it has been designed for the *value* of residual vibration rather than the percentage.

Another way to visualize input shaper performance is to examine vibration suppression over a range of liquid depths. Figure 31 shows the frequency of the first sloshing mode as

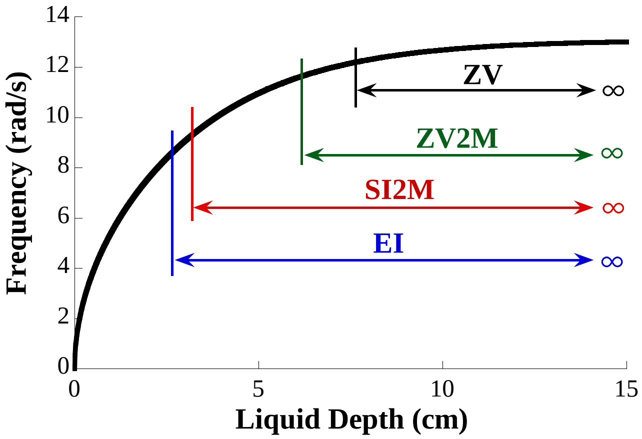

Figure 31. First Mode Slosh Frequency vs. Liquid Depth

a function of liquid depth. The range of acceptable vibration suppression for each input shaper is shown. For the ZV, EI, and ZV2M shapers, the acceptable range is the region of 5% suppression. The ZV shaper suppresses vibration at all liquid depths $>$ 7.9 cm. The ZV2M shaper performs slightly better, suppressing vibration to below 5% at liquid depths $>$ 6.8 cm. The very robust EI shaper suppresses the first mode of slosh at liquid depths $>$ 2.7 cm. The acceptable region of the SI2M shaper is shown to be range of liquid depths it was designed to suppress vibration. In this case, the SI2M shaper suppresses vibration at liquid depths $>$ 3 cm.

A similar plot is shown in Figure 32 for the second mode of slosh. The ZV and EI shapers are unable to suppress this higher mode. The SI2M produces acceptable vibration at all liquid depths $>$ 3 cm. The ZV2M shaper suppresses second mode vibrations to 5% at all liquid depths $>$ 2.5 cm. Note that the second mode frequency approaches the theoretical maximum more quickly than the first mode frequency.

4.5 Simulation Results

Simulations were conducted using a four-mode model and the testing parameters given in Table 2. Simulation results for a liquid depth of 12 cm are shown in Figure 33. The

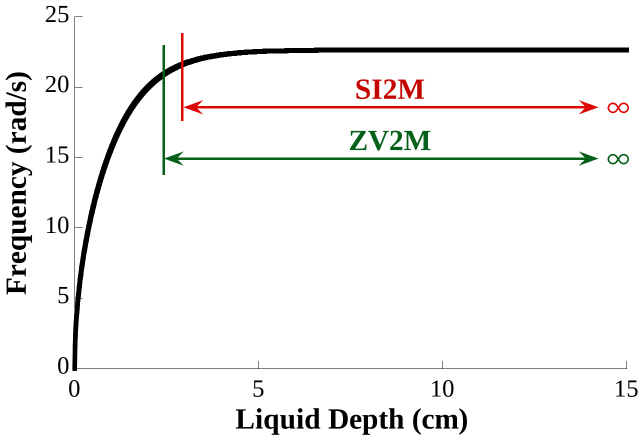

Figure 32. Second Mode Slosh Frequency vs. Liquid Depth

transient period (when the container is in motion) and the residual period (when the container is stopped) are marked. Figure 33(a) shows that the ZV- and EI-shaped commands suppress the first mode, but the remaining modes generate residual vibration amplitudes of 12 mm and 11 mm, respectively. However, these are far less than the 38 mm residual vibration amplitude of the unshaped command. Figure 33(b) shows that the ZV2M- and SI2M-shaped commands suppress the first two modes and produce low residual vibration amplitudes of only 5 mm. The SI2M case stayed within its design constraint of less than 10 mm of residual vibration. The 3-4-5 and 4-5-6-7 polynomial profiles in Figure 33(c) eliminate the high frequency content of the response, but the first mode remains, resulting in residual vibration amplitudes of 12 mm and 14 mm, respectively. The residual vibration amplitudes are listed in Table 4.

Simulations were also conducted for a liquid depth of 4 cm, and the results are shown in Figure 34. The system frequencies are lower at this depth compared to the 12 cm case, and the unshaped command induces a greater residual vibration amplitude (55 mm) than the 12 cm case. Figure 34(a) shows that the ZV-shaped command resulted in larger residual vibrations (22 mm) than the 12 cm case. However, the robust EI-shaped command suppressed the first mode and produced a result similar to the 12 cm case (10 mm). The ZV2M-shaper in Figure 34(b) suppressed most of the second mode vibrations, but the first

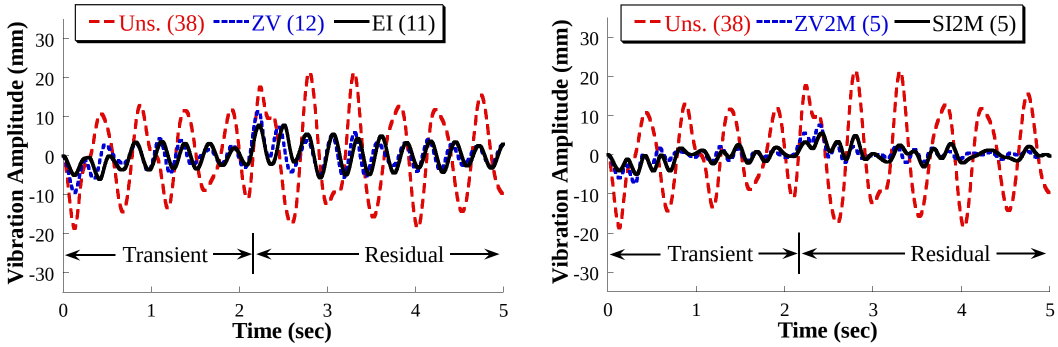

(a) One-Mode Shapers (b) Two-Mode Shapers

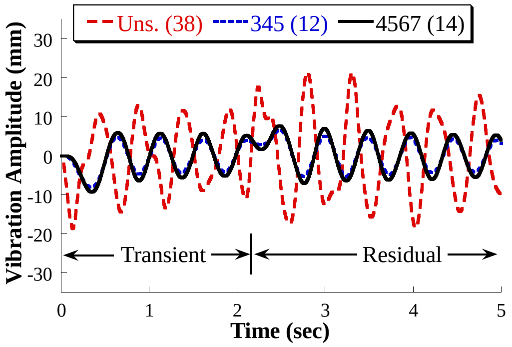

(c) Polynomial Profiles

Figure 33. Simulation Results from 12 cm Liquid Depth

Table 4. Residual Vibration Amplitude Simulation Results

Command	12 cm Depth		4 cm Depth	
	mm	% of Unshaped	mm	% of Unshaped
Unshaped	38	100%	55	100%
ZV	12	32%	22	40%
EI	11	29%	10	18%
ZV2M	5	13%	12	22%
SI2M	5	13%	6	11%
3-4-5	12	32%	30	55%
4-5-6-7	14	37%	34	62%

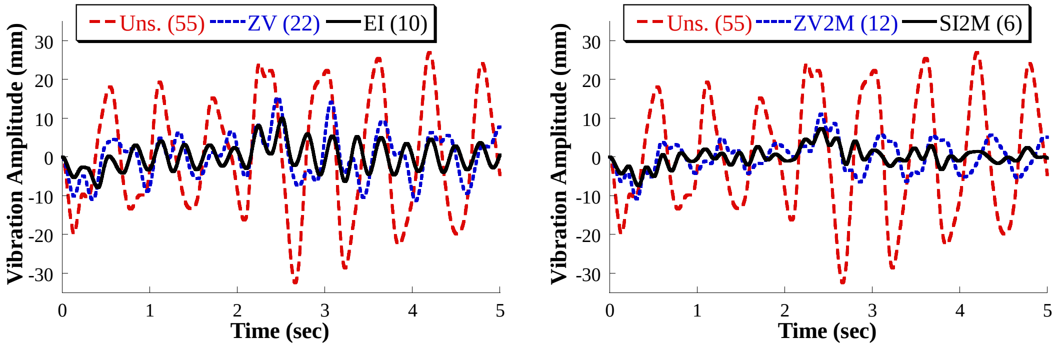

(a) One-Mode Shapers (b) Two-Mode Shapers

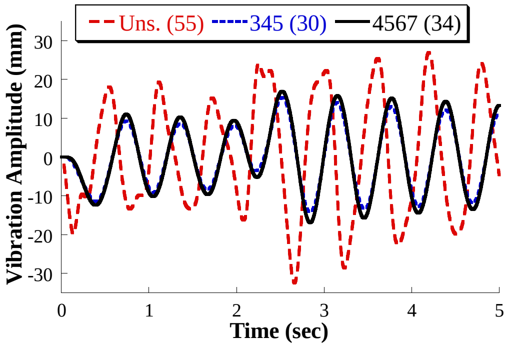

(c) Polynomial Profiles

Figure 34. Simulation Results from 4 cm Liquid Depth

mode contributed to the residual vibrations (12 mm). The SI2M shaper remained within its design constraint of less than 10 mm of residual vibration (6 mm). Although the 3-4-5 and 4-5-6-7 polynomial profiles in Figure 34(c) have rise times equal to that of the SI2M shaper duration, they induced substantially larger amounts of residual vibrations (30 mm and 34 mm, respectively).

These results highlight the design objectives of the four input shapers. At the deep liquid depth where slosh frequency varies only slightly, the one-mode shapers suppressed the first mode. The two mode shapers achieved additional slosh suppression by reducing residual vibration amplitude contributions from the first and second modes. At a shallow liquid depth, the robust shapers performed better than the non-robust shapers. These studies provide a basis for selecting an optimal input shaper for an application. For example, the ZV shaper was the fastest shaper and is most effective in a system that requires one mode of vibration suppression and has a non-changing, deep liquid depth. However, the slightly slower SI2M shaper can be used to accommodate large changes in liquid depth and suppression of the first two modes. These results also show that the polynomial profiles do not provide satisfactory slosh suppression with a rise time equal to the SI2M shaper at the deep and shallow liquid depth.

4.6 Experimental Results[1]

Experimental testing was conducted on the testing apparatus in Figure 28 using the parameters in Table 2 and the commands described in Section 4.4. Images of the residual vibrations at a liquid depth of 12 cm are shown in Figure 35. The unshaped case had large amplitude vibrations. The ZV-shaped case reduced vibrations, but two peaks of the second mode are visible. The ZV2M-shaped case further reduced residual vibrations, and the third mode shape is visible in these images. The 3-4-5 polynomial profile case had large amplitude vibrations in the first mode. The EI-shaped, SI2M-shaped, and 4-5-6-7 polynomial cases are not shown because they are similar to the ZV-shaped, ZV2M-shaped, and 3-4-5 polynomial cases, respectively.

A plot of the entire surface as a function of time for 12 cm unshaped case is shown in Figure 36. Between 0 and 1 seconds, the entire surface is level and not moving. The container accelerates at 1 second which induces slosh, and the container decelerates 2 seconds later which induces additional slosh. This transient period is colored gray. The residual slosh has an amplitude of 28 mm and damps out over time ($\zeta_1 \approx 0.10$). A similar plot for the 12 cm SI2M-shaped case is shown in Figure 37. The residual slosh amplitude is reduced to 5 mm. Because the first and second modes have been nearly eliminated, the movement of the third mode shape is revealed in the surface. Plots for the other tests are provided in Appendix C.

To better identify the modal contributions, the Fast Fourier Transform (FFT) of each

---

[1] ***Work in this section was done in conjunction with Mr. Kun Bai***

(a) Unshaped

(b) ZV Shaped

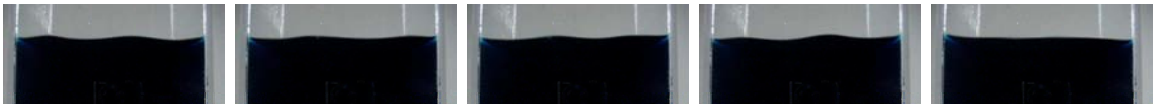

(c) ZV2M Shaped

(d) 3-4-5 Polynomial Profile

Figure 35. Experimental Testing Images from 12 cm Liquid Depth

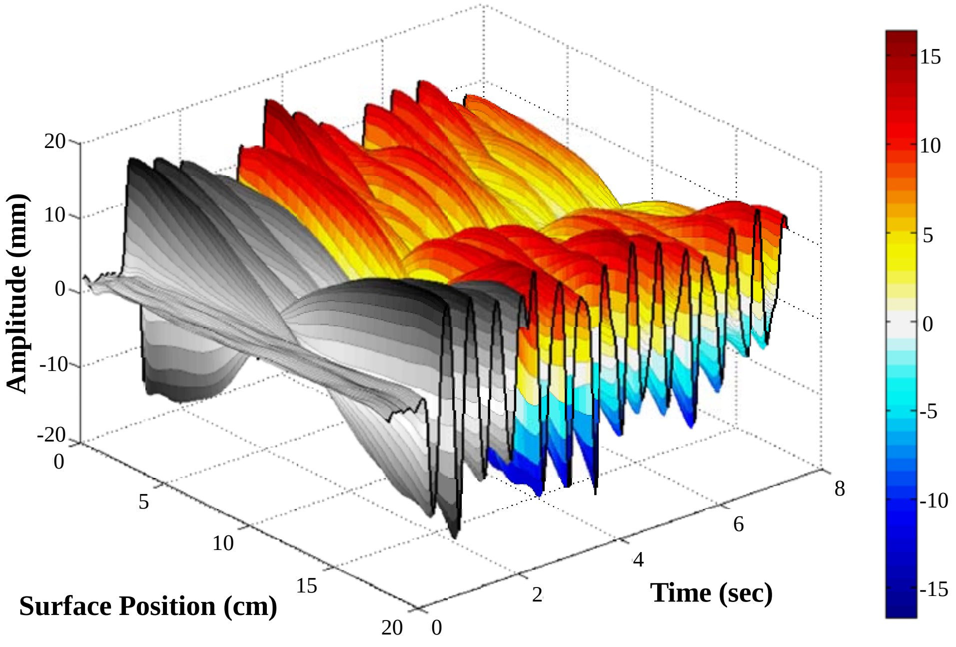

Figure 36. Surface Oscillations for 12 cm Unshaped Case

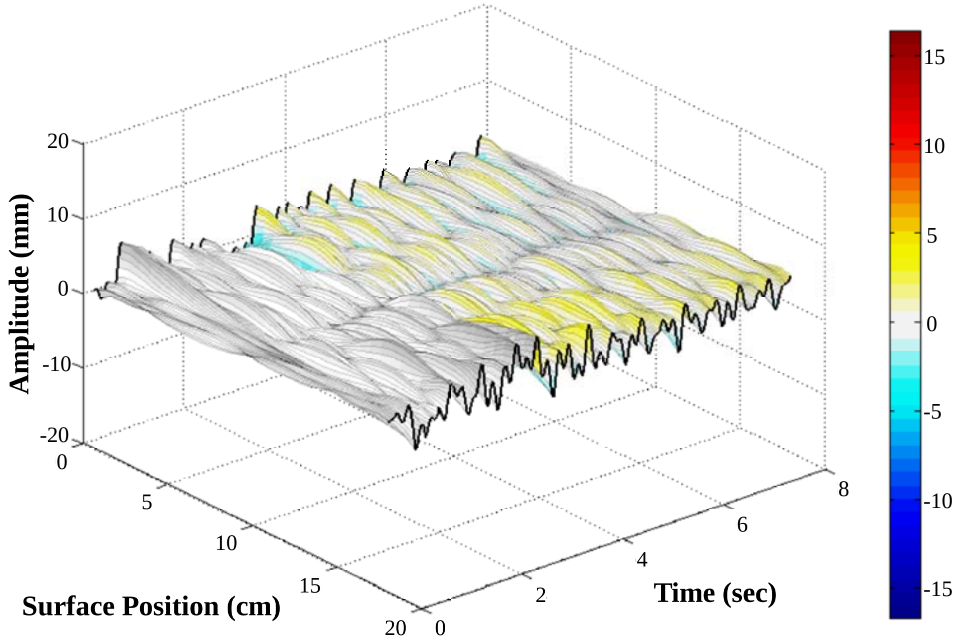

Figure 37. Surface Oscillations for 12 cm SI2M-Shaped Case

result from the 12 cm case is shown in Figure 38. The first and second mode frequencies are revealed by the peaks of the unshaped case at 13 rad/s and 23 rad/s, respectively. The ZV- and EI-shaped commands reduced the magnitude at the first frequency, but the second frequency magnitude remained large. The ZV2M- and SI2M-shaped cases reduced the magnitude of both the first and second frequencies. The low-pass filtering effect of the 3-4-5 and 4-5-6-7 polynomial profiles did not reduce the magnitude at the first mode frequency, but the higher modes of vibration were attenuated.

Next, testing was conducted for liquid depths from 2 to 12 cm in increments of 1 cm. The residual vibration induced by all commands and liquid depths are shown in Figure 39. The unshaped command caused the greatest residual vibrations at all liquid depths. The polynomial profiles produced the second and third greatest residual vibrations at all liquid depths except for the 6, 7, and 8 cm cases. The 4-5-6-7 profile induced greater vibrations than the 3-4-5 profile, which agrees with the results in Chapter 3. The residual vibrations caused by the unshaped command and polynomial profiles varied across liquid depths because of interference between vibrations induced by the 'go' and 'stop' commands.

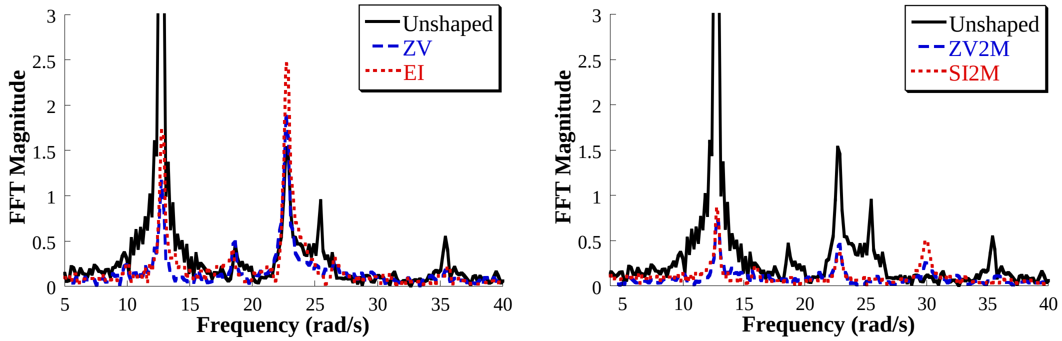

(a) One-Mode Shapers

(b) Two-Mode Shapers

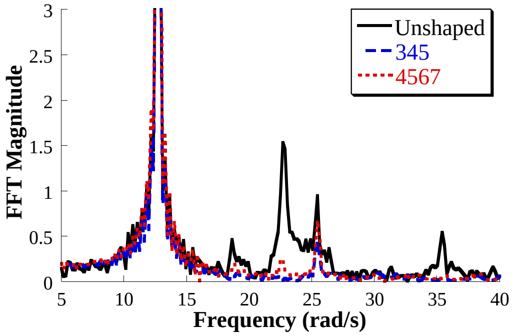

(c) Polynomial Profiles

Figure 38. FFT of Experimental Results from 12 cm Liquid Depth

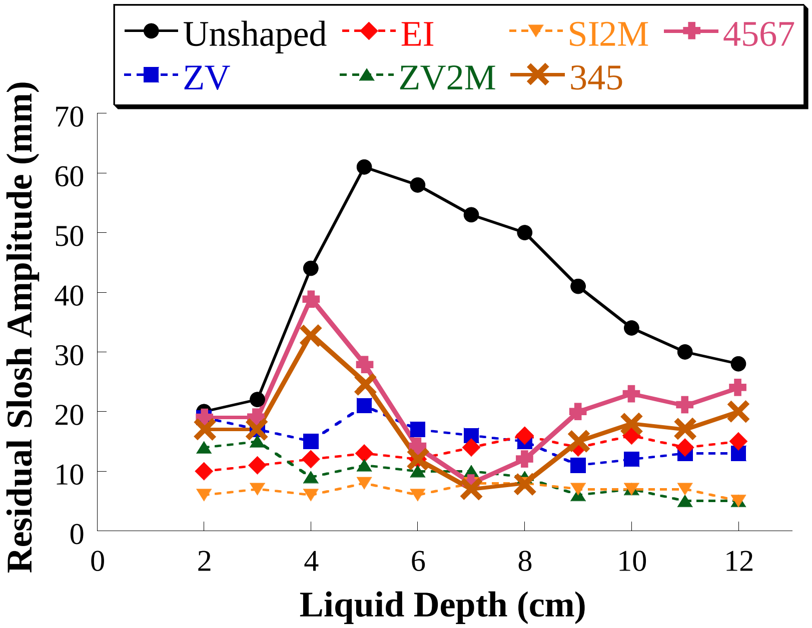

Figure 39. Experimental Testing Results

The input-shaped commands succesfully reduced the residual vibrations. The ZV- and EI-shaped commands produced similar results at deep liquid depths. However, as the frequency changed at shallower liquid depths, the slosh induced by the ZV-shaped command increased relative to that induced by the EI-shaped command. This confirms the relative robustness of the EI shaper. The ZV2M- and SI2M-shaped commands also produced similar results at deep liquid depths. At shallow liquid depths, the ZV2M-shaped command produced its greatest residual vibrations. The SI2M-shaped command remained robust to changes in liquid depth and limited residual vibrations to less than 10 mm for all cases. Note that the shaped commands reduced the effect of interference between the vibrations induced by the 'go' and 'stop' commands because input shaping suppressed vibrations induced by each command separately.

The FFT of each result from the 4 cm case is shown in Figure 40. At this liquid depth, the first and second mode frequencies are 10 rad/s and 22 rad/s, respectively. In Figure 40(a), the ZV-shaped command had a greater magnitude at the first frequency than the robust EI-shaped command, and both commands had similar magnitudes at higher frequencies. In Figure 40(b), the ZV2M-shaped command also produced a greater magnitude at the first frequency than the robust SI2M-shaped commands. In Figure 40(c), the polynomial profiles were unable to significantly attenuate the first and second frequencies.

To better examine the robustness of each command to changes in liquid depth, Figure 41 shows the FFT for both the 12 cm and 4 cm liquid depths in the same plot for each command. The FFT of the unshaped result had an average peak magnitude of 6.8 at the first mode and an average peak magnitude of 1.8 at the second mode. The ZV-shaped command reduced the magnitude at the first mode, but the 4 cm case had a larger magnitude because the ZV shaper is not robust to changes in frequency. The robust EI-shaped command reduced the magnitude of the first mode for the 12 cm case, and greatly reduced the magnitude for the 4 cm case. Because the ZV- and EI-shaped commands could not suppress the second slosh mode, they had large magnitudes at the second mode for both liquid

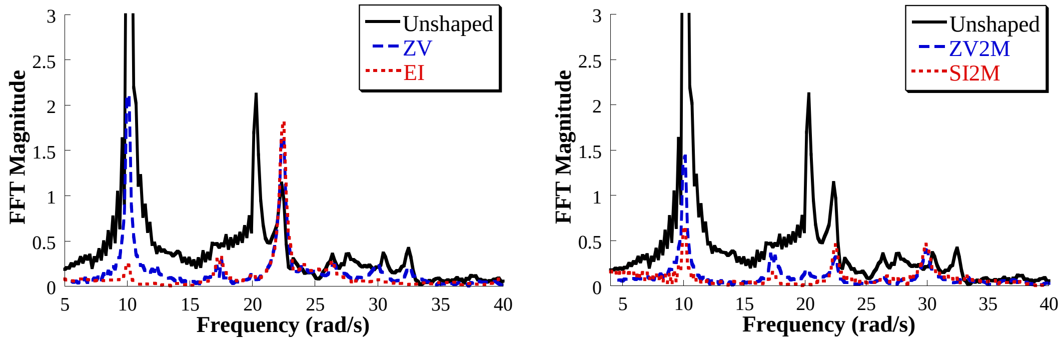

(a) One-Mode Shapers (b) Two-Mode Shapers

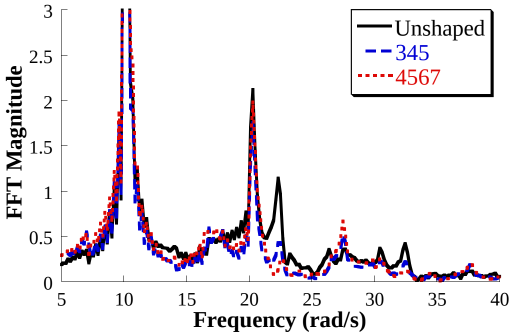

(c) Polynomial Profiles

Figure 40. FFT of Experimental Results from 4 cm Liquid Depth

depths. The ZV2M-shaped command had a larger magnitude for the 4 cm case than the 12 cm case because it is not robust to frequency changes. However, the SI2M-shaped command is robust at the first mode and had very small magnitudes for both liquid depths. The ZV2M- and SI2M-shaped commands equally reduced the magnitude at the second mode for both liquid depths. The low-pass filtering effect of the 3-4-5 and 4-5-6-7 polynomial profiles is also demonstrated: the first mode magnitudes were similar to the unshaped case, and the second mode magnitudes were attenuated.

These experiments verify the key results predicted by the simulations. Robust input shaping suppressed vibration over a range of system frequencies, and two-mode input shaping suppressed vibration of the second mode of slosh. In addition, these results show that polynomial profiles were not an effective method to suppress slosh with a fast rise time. Although the polynomial profiles peformed better than input shaping in some cases, this vibration suppression is not repeatable for a range of system frequencies or move distances.

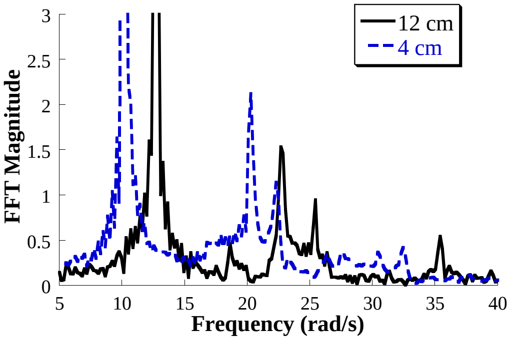

(a) Unshaped

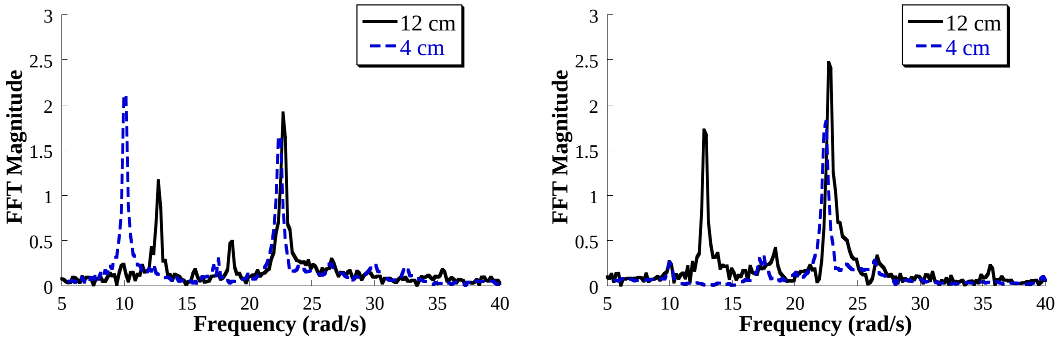

(b) ZV-Shaped

(c) EI-Shaped

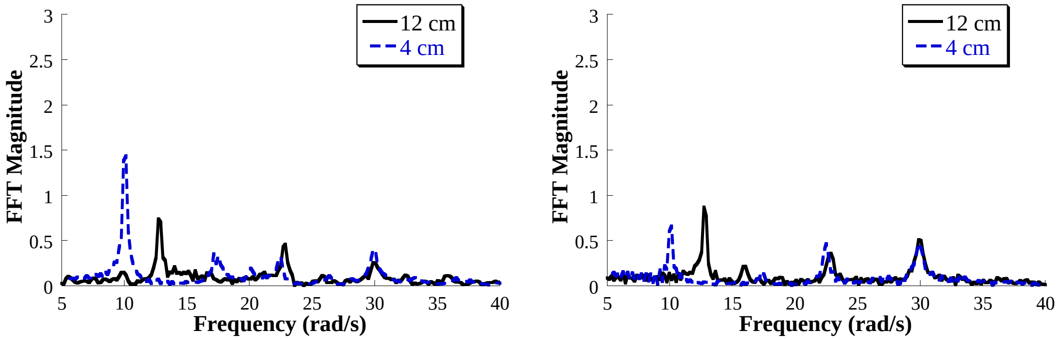

(d) ZV2M-Shaped

(e) SI2M-Shaped

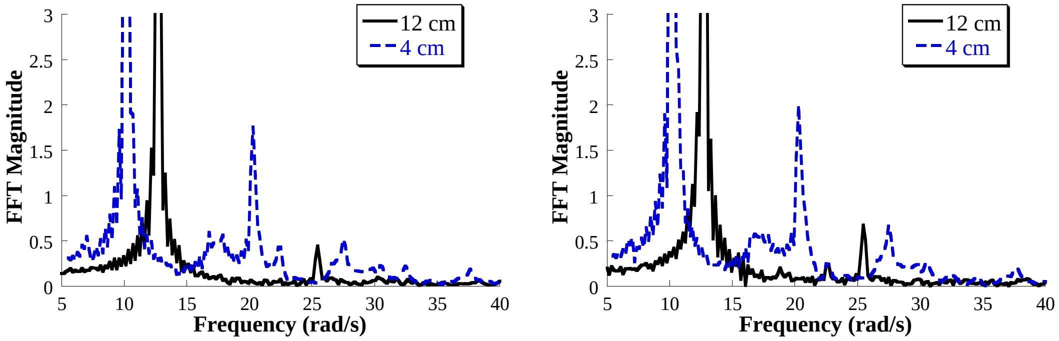

(f) 3-4-5 Polynomial

(g) 4-5-6-7 Polynomial

Figure 41. FFT of Experimental Results from 4 cm Liquid Depth

CHAPTER V

CHERRYPICKER

Aerial lifts raise people high up in the air so that they can work on power lines, buildings, airplanes, and similar elevated structures [40, 84, 85]. Figure 42 shows an aerial lift that uses a scissor mechanism to extend straight upwards. Figure 43 shows a different type of aerial lift, often called a cherrypicker. This type of lift uses a jointed arm to extend not only upward, but also out from the truck that forms its base.

The cherrypicker has a much larger workspace than the scissor lift, but given that it can extend out from the base, it will oscillate, and can even tip over [12, 48]. Oscillations of the workers can cause work delays, injuries, and property damage. Examples include when the bucket oscillates into a glass-sided building and when the bouncing bucket forces workers close to power lines. If the machine tips over, then the result can be catastrophic. For example, the cherrypicker shown in Figure 43 tipped over at the Miami airport when the workers where installing an antenna on the tail of a DC-8 airplane. One of the workers died and the other was severely injured.

A small-scale cherry picker has been constructed for use as an experimental and educational testbed. During the Fall 2010 semester, an advanced controls course at the Massachusetts Institute of Technology (MIT) used the machine in several laboratory exercises. This chapter presents details of the mechanical design and control system of the small-scale cherrypicker. Then, the system is used to compare the effectiveness of polynomial profiles and input shaping.

Figure 42. Scissor Lift

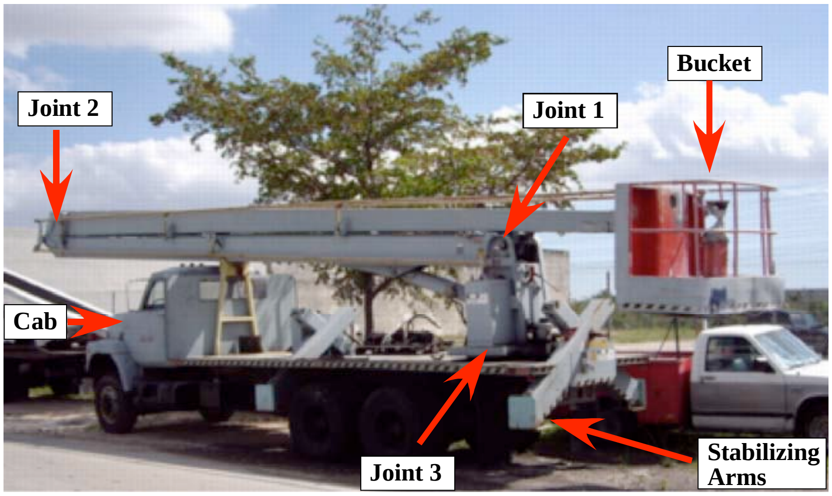

Figure 43. Cherrypicker Involved in Fatal Accident at Miami Airport

5.1 Mechanical Design[1]

The house of quality in Figure 44 was created to determine which features of the cherrypicker were most integral to its successful operation and to ensure that customer needs were addressed by the design. The left-hand column lists customer needs - qualities that

---

[1] *Work in this section was done in conjunction with Mr. Ehsan Maleki and Mr. Lukas Kaufmann*

are desired in the finished product. In this case, the primary customers are students using the cherrypicker for class and the professors teaching the class. The column adjacent to the customer needs gives the relative importance of each feature to the customer. Safe operation and a flexible control system are two of the most important features to the customers. The top row lists engineering requirements - features that can be controlled by the engineering design team.

The central matrix of the house of quality gives a correlation between the customer needs and the engineering requirements, where 1 is a low correlation and 5 is a high correlation. For example, the base design has a large influence on the size and variable inertia properties. The webcam has a strong influence on the tele-operation capabilities, but it has little bearing on other customer needs. To determine the most important engineering requirements, each number in the matrix is multiplied by the importance, and the sum of each column is calculated. The interface ease of use and base design were determined to be the most important engineering requirements to satisfy customer needs. This is a reasonable result because the interface must provide clear and simple access to all capabilities of the cherrypicker, and the base design is the foundation for all of the mechanical components.

The ‘roof’ of the house of quality examines how the engineering requirements impact each other. Four symbols are used to give the correlation between each engineering requirement. This analysis helped determine tradeoffs and synergies of the engineering requirements. For example, a large base can increase the workspace size but will have detrimental effects on the weight of the machine.

Several designs were developed based on the house of quality results and were systematically evaluated. The final design is sketched in Figure 45. The base measures approximately 1 m by 0.5 m. The slew motor is mounted to the base and rotates the turntable via a worm gear. The shoulder motor is mounted to the central post and actuates the shoulder joint through a timing belt and pulley. The elbow motor is mounted at the first arm

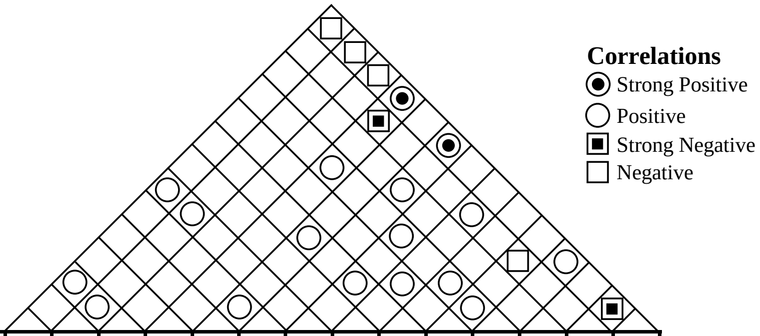

Customer Needs	**Importance**	Slew Speed	Luffing Speed	Luffing Arm Flexibility	Base Design (Geometry, Material)	Interface Ease of Use	Webcam (Location, Pitch/Rotate)	Sensors (Size, Location, Accuracy)	Power System	Control System	Number of Components	Stabilizer	Network Capability	Lightweight	Workspace Size
Small Footprint	6			3	5						1	1		5	5
Five Degrees of Freedom	8					3		3	3	3	5	3			1
State Measurements	9	1	1	3				5			1				
Flexible Control System	10	1	1	3		3				5			1		
Stability Measurement	8	1	1	1	3			5		3		5			
Simple User Interface	7					5		1		3					
Tele-Operation	8	1	1			5	5			3			5		1
Variable Inertia Properties	5				5						1			1	
Durable	8			3	3						5			3	
Transportable to MIT	8				5				3		5			5	3
Safe Operation	10	3	3	1	3	1			1			3			1
Information Acquisition	8					5				3			3		
Easily Powered	7	1	1					1	5				1		
Simple Design	7				5	3			3		5	1		1	1
Large Workspace	7	1	1	1	1		3				1			3	5
Column Σ		9	9	15	30	25	8	15	15	20	24	13	10	18	17
Σ(Importance*Relationship)		79	79	144	215	220	91	153	134	197	212	107	111	157	142
Relative Value {Σ/TotalΣ}		0.04	0.04	0.07	0.11	0.11	0.04	0.07	0.07	0.10	0.10	0.05	0.05	0.08	0.07

Engineering Requirements

Figure 44. Cherrypicker House of Quality

attachment point and also transmits power through a timing belt and pulley. The shoulder motor gearbox provides a 50:1 speed reduction, and the elbow motor gearbox provides a 20:1 speed reduction. The two arms are constructed from 1 m sections of a pole vault pole.

The constructed cherrypicker is shown in Figure 46. Each motor is equipped with an encoder that outputs velocity and absolute position. The endpoint of the cherrypicker

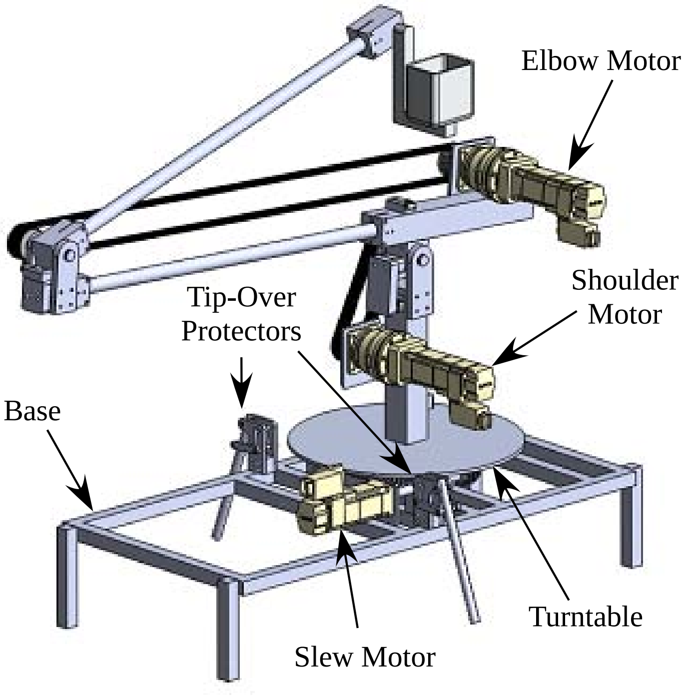

Figure 45. SolidWorks Image of Cherrypicker

is tracked by a machine vision system, and the horizontal and vertical positions of the endpoint are recorded.

In addition to these features, other design considerations facilitate its use as an experimental and educational testbed. To reduce the overall weight, the majority of the components are aluminum and the motors were selected to provide sufficient power while minimizing weight. T-slotted framing was used due to its light weight and ease of assembly. It was also used for the shoulder and elbow motor mounting points. In this way, the timing belts could be tensioned without the use of a tensioner or idler pulley.

The worm gear in Figure 47 transmits power for the slewing motion. This eliminates the need for a gear box on the slew motor while also providing reliable, slip-free motion. A flexible coupling accommodates slight errors in alignment, and a pillow block bearing supports the shaft. The timing belt for the shoulder joint is made of a stronger, more expensive material than the timing belt for the elbow joint because it requires a greater tension. The pulleys for the elbow motion were placed close to the arm to minimize the

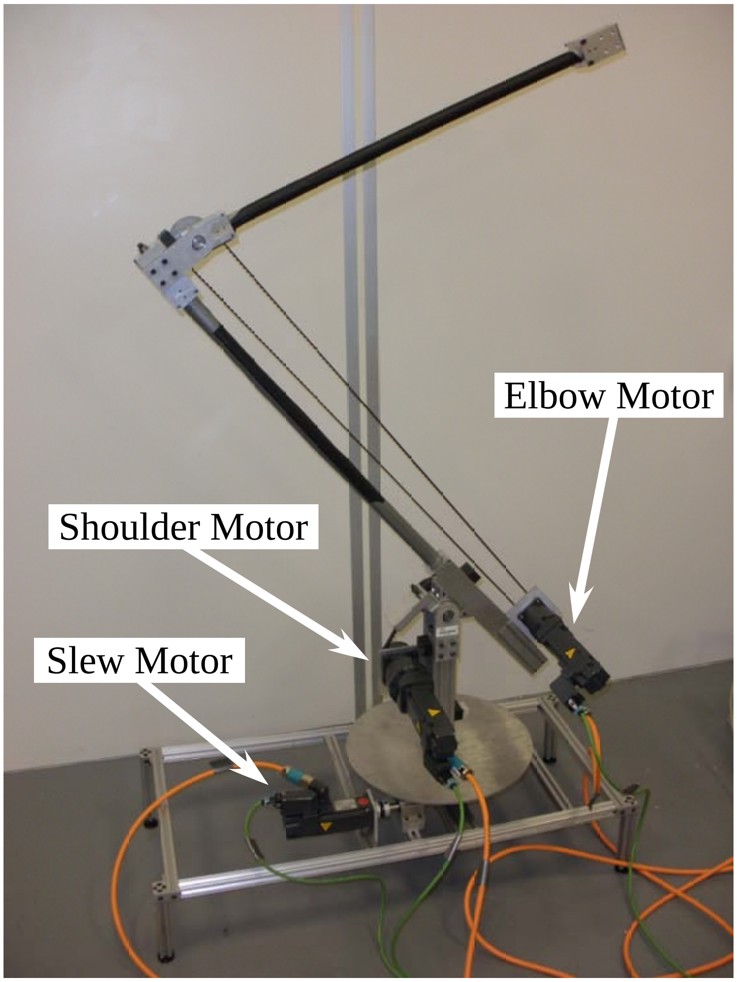

Figure 46. Constructed Cherrypicker

bending moment on the pole. They also provide a 2:1 speed reduction for a total speed reduction of 40:1 at the elbow joint.

The inertial properties of the cherrypicker can be varied, and safety measures are included in the event of a tip-over. The legs can be moved to change the footprint size, and the arms can be replaced to provide more or less flexibility and weight. Additional legs that swing out from the base protect the machine from completely tipping over. Figure 48 provides a demonstration of this feature. Under normal operating conditions, the leg remains upright and the pin rests at the top of the slot as seen in Figure 48(a). When the cherrypicker begins to tip over, gravity pulls the pin down the slot which extends the leg, as shown in Figure 48(b). The pin remains locked in place and prevents the cherrypicker

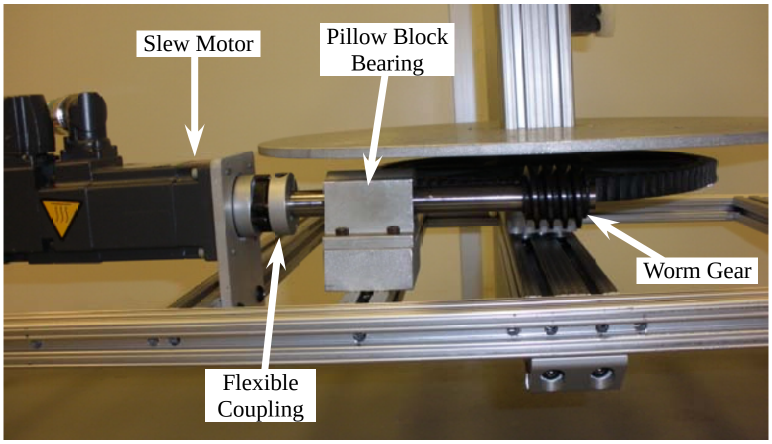

Figure 47. Slew Motor and Worm Gear

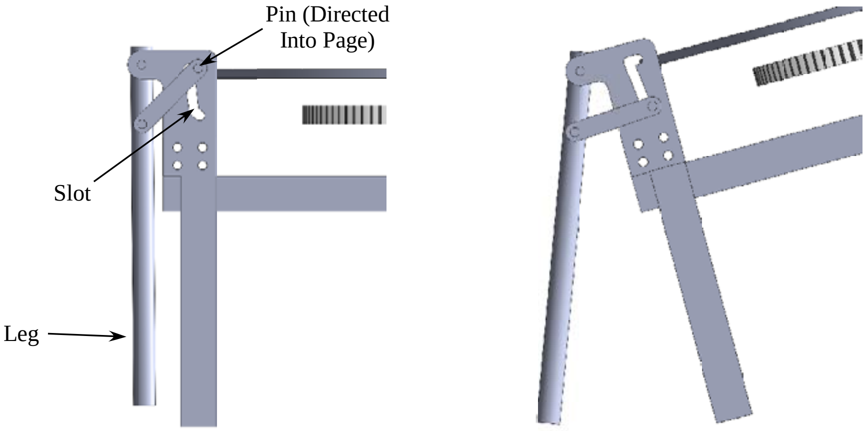

(a) Stable Cherrypicker Configuration (b) Tipped-Over Configuration

Figure 48. Tip-Over Protector Demonstration

from tipping further.

The graphical user interface (GUI) used to control the machine motion is shown in Figure 49. The top left area contains the buttons to control each direction of rotation. The bottom left area provides several options to the user. The type of input shaper can be selected; a pre-planned trajectory can be uploaded and executed; velocity and position data can be recorded and downloaded; and the control directions can be changed to a different coordinate system. The right side of the GUI contains the real-time position of the

base angle -11
shoulder angle 25
elbow angle 24
cam x 0
cam y 0
cam2 x 171
cam2 y 654
current shaper Unshaped

Figure 49. Cherrypicker GUI

cherrypicker from both top and side views. The angle of each joint is displayed, and dynamic figures provide tele-operators with an image of the cherrypicker configuration. The machine vision output is also displayed.

Additional methods of operation are also provided. The operator control box in Figure 50 provides alternate control inputs. Three joysticks control the three degrees of freedom. Several buttons were included to provide access to other control features. Remote operators can connect to the control interface through a Virtual Network Computing connection, and a webcam can be accessed to view the machine.

The cherrypicker was used in a course at MIT titled, ”Command Shaping: Theory and Applications” during the Fall 2010 semester. The MIT students used the cherrypicker for a series of laboratory exercises to supplement their classroom experience. As a result, the cherrypicker met most design goals and provides the foundation to reach other objectives in the future. The three motors provided realistic motion of the cherrypicker, and the machine vision gave accurate measurements of the endpoint position. The GUI was simple to learn

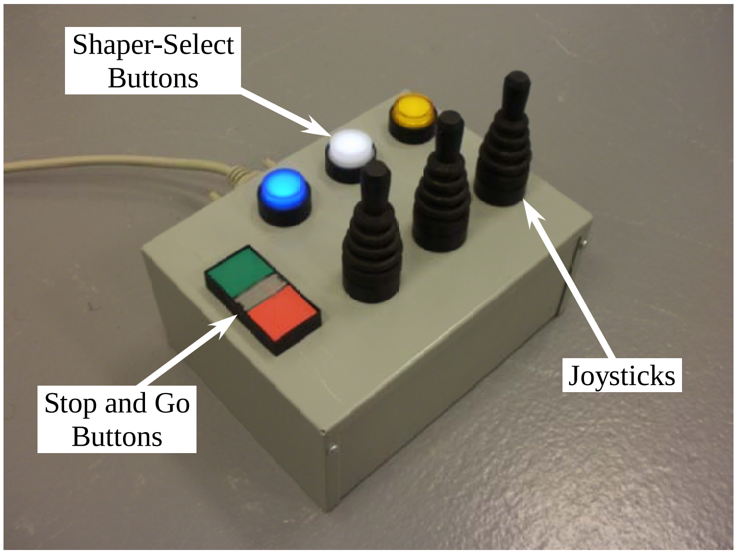

Figure 50. Cherrypicker Control Box

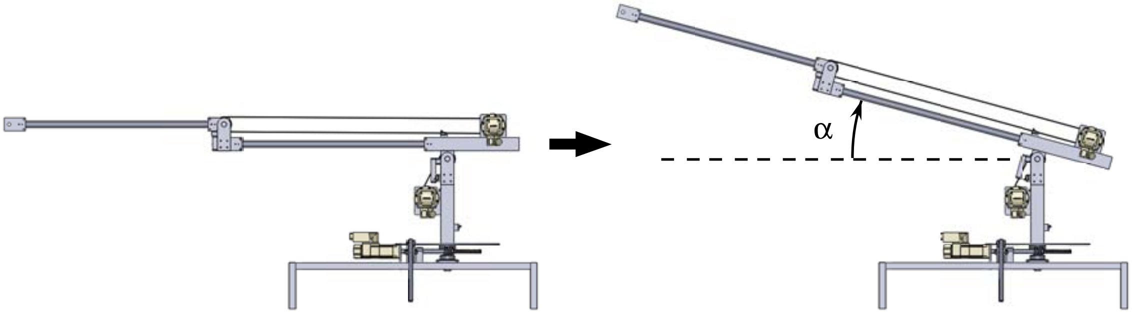

Figure 51. Side View of Cherrypicker Showing Shoulder Joint Motion

and use, and also allowed students to test implement advanced control techniques. The primary objective for future work is to reduce the weight to facilitate the safety of tip-over dynamics experiments.

5.2 *Experimental Results*

The natural frequency and damping ratio of the cherrypicker were experimentally determined while the cherrypicker was in the extended state, shown on the left of Figure 51. In this configuration, the frequency was determined to be approximately 2 Hz, and the damping ratio was calculated to be 0.08 from the logarithmic decrement.

Table 5. Shaper Impulse Amplitudes and Times

ZV	t_i	0	0.200	
	A_i	0.56	0.44	
SI	t_i	0	0.261	0.519
	A_i	0.33	0.46	0.21

Unshaped, ZV-shaped, and SI-shaped trapezoidal-velocity commands were tested on each joint of the small-scale cherrypicker. The ZV shaper was designed using the experimentally determined parameters in the extended configuration ($f = 2$ Hz, $\zeta = 0.08$). The SI shaper was designed to suppress frequencies between 1.5 and 2 Hz to 5% residual vibration. This range was selected because if the endpoint mass increases (e.g. people and tools loaded into an empty bucket), then the system natural frequency decreases. This SI shaper can accommodate a 25% decrease in system frequency that the non-robust ZV shaper cannot accommodate. The impulse amplitudes and times of these two shapers are given in Table 5. In addition, 3-4-5 and 4-5-6-7 polynomial profiles with rise times equal to the duration of the SI shaper were also designed.

The shoulder joint was moved while the elbow joint remained stationary and fully extended. This motion is illustrated in Figure 51. The position of the endpoint for a 15° shoulder joint motion is shown in Figure 52. The unshaped move caused a residual vibration amplitude of 33 mm. The ZV- and SI-shaped commands reduced the residual vibration to 10 and 12 mm, respectively. The 3-4-5 and 4-5-6-7 polynomial profiles reduced the residual vibration only slightly to 25 and 27 mm, respectively. Consistent with the results seeen in Chapter 3, the 4-5-6-7 profile induced somewhat greater vibrations than the 3-4-5 profile. These residual vibration amplitudes are listed in the second column of Table 6.

Larger shoulder joint motions of 30° and 45° were also tested, and the results are listed in Table 6. At different move distances, the commands induced different amounts of residual vibration due to interference between the vibration induced by the acceleration and deceleration portions of the commands. The ZV- and SI-shaped commands consistently

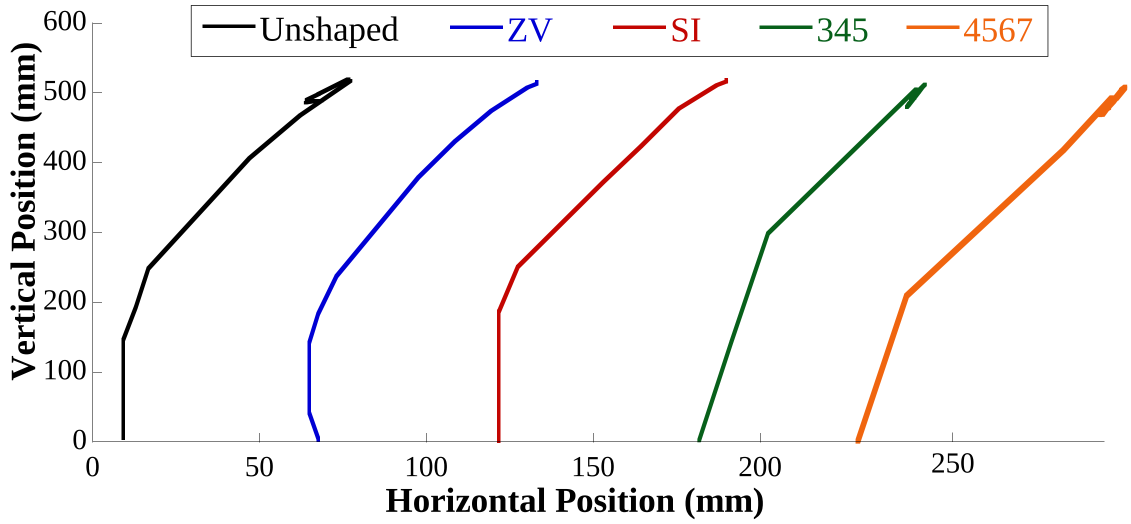

Figure 52. Endpoint Vibration for 15° Shoulder Joint Motion, Unweighted Endpoint

Table 6. Endpoint Residual Vibration Amplitude Due To Shoulder Joint Motion

Command	Unweighted (mm)			Weighted (mm)		
	15°	30°	45°	15°	30°	45°
Unshaped	33	41	58	132	103	108
ZV	10	12	27	106	47	92
SI	12	21	23	22	15	26
3-4-5	25	62	35	67	53	40
4-5-6-7	27	68	35	84	88	35

reduced the vibration relative to the unshaped command. It is interesting to note that the two polynomial profiles induced more vibration than the unshaped command for the 30° move.

To study changes in the cherrypicker dynamics when the payload mass increases, the mass was increased by 50%. This lowered the system natural frequency by approximately 20%. The position of the endpoint for the 15° shoulder joint motion is shown in Figure 53, and the residual vibrations amplitudes are listed in the fifth column of Table 6. The unshaped case had larger residual vibrations than the unweighted case. The ZV-shaped case also had large residual vibrations because it is not robust system frequency changes.

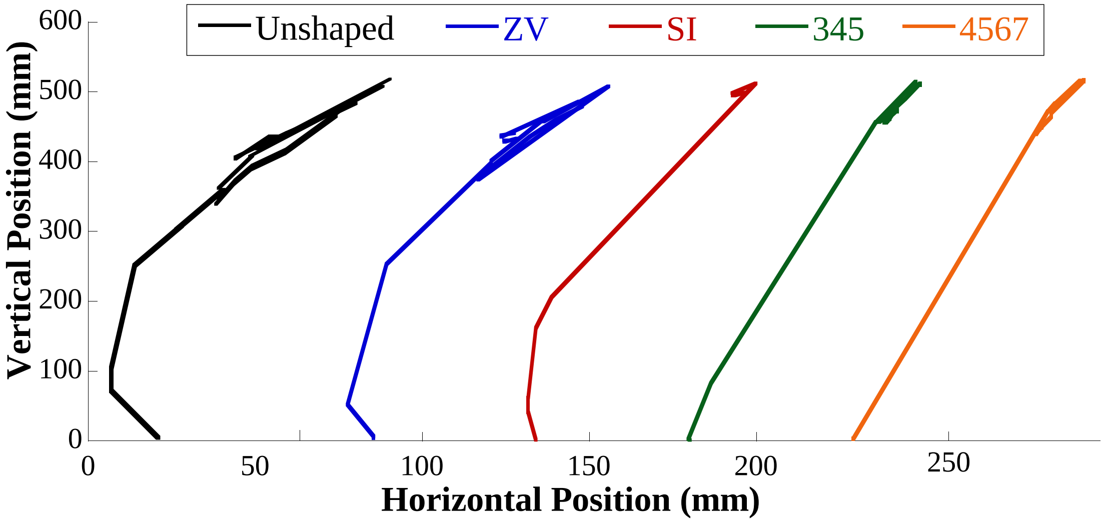

Figure 53. Endpoint Position for 15° Shoulder Joint Motion, Weighted Endpoint

However, the robust SI-shaped command reduced vibrations to a similar level as the unweighted case. The polynomial profiles induced much larger vibrations than the SI case despite having equivalent rise times.

As a result, the ZV-shaped command reduced the residual vibration amplitude from the unshaped command by an average of 63% for the unweighted case and an average of 29% for the weighted case. The SI-shaped command reduced residual vibration for the unweighted case by 58% and for the weighted case by 82%. The 3-4-5 and 4-5-6-7 polynomial profiles reduced residual vibration by 8% and 2% for the unweighted case, respectively, and by 53% and 40% for the weighted case, respectively. Despite having a rise time equal to the duration of the SI shaper, the polynomial profiles were unable to provide the same performance improvement as the SI-shaped command for these shoulder joint motions.

Similar studies were conducted for the elbow joint. Motions of 36°, 48°, and 60° were tested using the five commands while the shoulder joint remained stationary. This motion is illustrated in Figure 54. As the elbow contracts, the cherrypicker dynamics change, and the system frequency was observed to increase slightly. The residual vibration amplitudes from both unweighted and weighted cases are given in Table 7. The residual vibrations induced

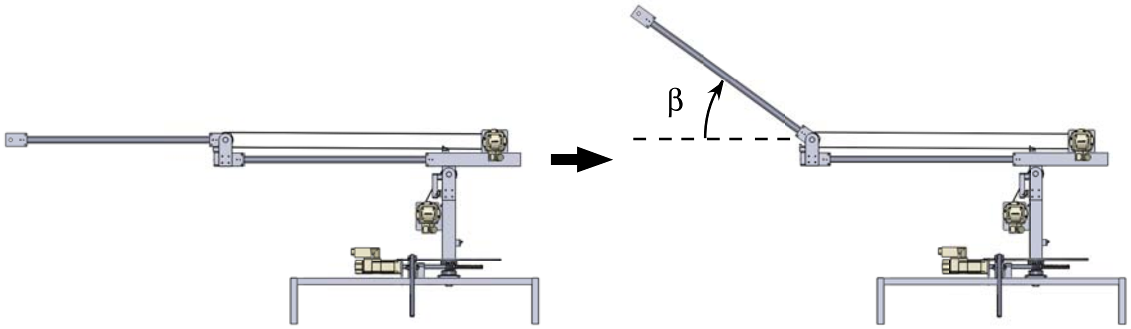

Figure 54. Side View of Cherrypicker Showing Elbow Joint Motion

Table 7. Endpoint Residual Vibration Amplitude Due To Elbow Joint Motion

Command	Unweighted (mm)			Weighted (mm)		
	36°	48°	60°	36°	48°	60°
Unshaped	15	50	23	51	47	18
ZV	11	10	11	26	15	13
SI	12	10	10	16	10	10
3-4-5	11	10	15	17	14	24
4-5-6-7	12	24	11	25	14	25

by the unshaped command were relatively large and varied across different move distances. The ZV- and SI-shaped commands suppressed vibration equally well in the unweighted case. The robust SI-shaped command performed better than the ZV-shaped command when weight was added to the endpoint. The polynomial profiles reduced vibration amplitude for the unweighted case, but performed worse than the SI-shaped command in the weighted case.

For these elbow joint motions, the ZV-shaped command reduced the residual vibration amplitude from the unshaped command by an average of 64% for the unweighted case and an average of 53% for the weighted case. The SI-shaped command reduced residual vibration for the unweighted case by 64% and for the weighted case by 69%. The 3-4-5 and 4-5-6-7 polynomial profiles reduced residual vibration by 60% and 57% for the unweighted case, respectively, and by 53% and 45% for the weighted case, respectively.

These results further confirm the advantages of input shaping over polynomial profiles. A non-robust ZV shaper suppressed residual vibration for two types of cherrypicker motion in a nominal case. To accommodate additional endpoint mass which decreased the system frequency, a robust SI shaper decreased residual vibrations in all cases. Although the 3-4-5 and 4-5-6-7 polynomial profiles reduced residual vibration in some cases, they did not consistently reduce vibration to the same level as input-shaped commands.

CHAPTER VI

CONCLUSIONS AND FUTURE WORK

Flexible systems are widespread and present a host of challenging engineering problems. Cranes, cherrypickers, sloshing liquids, and cam-follower systems all have flexible dynamics that limit their performance. When choosing a method of command shaping to improve the performance of these systems, it is important to consider both safety and efficiency. In other words, it is important to use a command with a rapid response time that also suppresses the flexible dynamic response. This thesis provided a comprehensive comparison between two methods of command shaping: polynomial profiles and input shaping.

In Chapter 2, polynomial profiles and input shaping were reviewed. Polynomial profiles are commonly used in cam-follower systems, and their ease of design has extended their use to other areas. It was shown that polynomial profiles provide a smooth transition between setpoints in a command. This command smoothing technique primarily provides a low-pass filtering effect in order to suppress vibrations. Input shaping was shown to more-directly target the flexible modes.

Chapter 3 provided a numerical comparison between polynomial profiles and input-shaped commands. It was shown that polynomial profiles do not contain an embedded input shaper, so the two methods have a fundamental difference. The rise time of polynomial profiles and input-shaped commands was compared. On average, polynomial profiles require a rise time three times as long as the rise time of basic input-shaped commands to achieve similar residual vibration suppression.

These results have practical implications. Through the use of input shaping, the throughput of a process that contains flexible components can be increased compared to a system using polynomial command profiles. Automated machinery, such as a pick-and-place machines, can complete a task more rapidly if they are driven by input-shaped commands.

Chapter 4 described the use of command shaping as a means to control slosh. The dynamics of slosh in a rectangular container were described. Four input shapers were designed to accommodate several scenarios, including: one- or two-mode suppression, and robust or non-robust performance. Two polynomial profiles were also designed with a rise time equivalent to the slowest of the input shapers. Simulations showed that one-mode input shapers decreased residual vibration amplitude compared to the unshaped case, and two-mode input shapers further decreased the residual vibration amplitude. Simulations also showed that robust input shapers can accommodate changes in slosh frequency associated with changes in liquid depth.

Experimental testing verified these results. The most notable success was a two-mode specified insensitivity shaper that limited residual vibration to below a specified amplitude at all liquid depths. In comparison, polynomial profiles did not consistently reduce the sloshing amplitude. For eight out of the eleven tests, the polynomial profiles produced greater residual vibration than all the input-shaped commands. The three cases where polynomial profiles reduced residual vibration could be attributed to interference between oscillations induced by the acceleration and deceleration parts of the command, and this vibration suppression is not repeatable for a range of system frequencies or move distances. These results further verify the conclusions of Chapter 3.

Chapter 5 described the design of a small-scale cherrypicker. Several design considerations were made in order to facilitate its use as an experimental and educational testbed. Students in coming years will be able to supplement their course work and research with this machine. Input-shaped commands and polynomial profiles were tested on the cherrypicker. The results from these tests also agreed with the conclusions of the previous chapters that input-shaped commands outperform polynomial profiles.

6.1 Future Work

To further demonstrate the benefits of input shaping, it would be advantageous to provide an objective comparison between input shaping and other smooth commands. The work presented here can be used as a basis for future analyses of smooth commands. Using the process described in Chapter 3, it can easily be determined if a smooth command does not contain an embedded input shaper. The simulation and experimental testing protocols presented in this thesis can then be peformed to compare additional smooth commands to input shaping.

Numerous real-world aspects of slosh remain to be studied. The extrapolation of the results in Chapter 4 to other container geometries and different types of liquid could be investigated to produce a large range of additional important results. Two-dimensional container motion and uncertainties in container length could also be studied. Deflection-limiting input shapers could be tested as a method to prevent spillage during the transient period. Input shaping should also be studied in the case of pouring liquid out of a container. Other studies, such as long move distances or slosh in large containers, may require a new experimental setup. Research into these areas can further demonstrate the effectiveness of input shaping in a wide range of slosh applications.

The cherrypicker provides a platform for many future investigations. Additional flexibility could be included in the arms to better reflect the two-mode response seen in cherrypickers and other two-arm manipulators. The weight of the cherrypicker could be reduced to improve the ease and safety of tip-over experiments. A system for measuring the end-point position in three dimensions should be developed. These improvements will greatly facilitate its use as an experimental and educational testbed in the future.

A number of studies remain that can encompass the wide range of operating conditions seen in cherrypickers. More comprehensive joint motions could be tested to examine the full dynamic range of the cherrypicker. Vibration control for slewing motions could also be studied. A flexible payload can be added to end point to simulate bucket sway. Static and dynamic stability conditions could be determined for different configurations of the joints and footprint. These studies could further show the benefit of input shaping as a method to improve cherrypicker safety.

APPENDIX A

INPUT SHAPER GENERALIZATION

An input shaper has n impulses with known amplitudes, A_i, and time spacings, t_i. The first impulse begins at $t_1 = 0$. To find the frequencies that are eliminated by an input shaper, the Laplace transform of the input shaper is set equal to zero:

$$A_1 + A_2 e^{-t_2 s} + \cdots + A_n e^{-t_n s} = 0 \tag{48}$$

Substituting $s = \sigma + j\omega$ and assuming no damping yields:

$$e^{-t_i s} = e^{-t_i(\sigma + j\omega)} = \cos \omega t_i - j \sin \omega t_i \tag{49}$$

Substituting (49) into (48) yields:

$$\frac{A_2}{A_1} \cos \omega t_2 + \cdots + \frac{A_n}{A_1} \cos \omega t_n = -1 \tag{50}$$

$$\frac{A_2}{A_1} \sin \omega t_2 + \cdots + \frac{A_n}{A_1} \sin \omega t_n = 0 \tag{51}$$

If (50) has a solution, then it must repeat at some constant period based on the least common multiple of the arguments. The same is also true for (51). The overall solution is the intersection of the real cosine and imaginary sine solutions. If an overall solution exists, then it too must repeat at some constant period based on the least common multiple of the arguments of the trigonometric functions.

APPENDIX B

POLYNOMIAL PROFILE GENERALIZATION

A function is converted to the frequency domain with a continuous Fourier transform (CFT), given by:

$$X(j\omega) = \int_{-\infty}^{\infty} x(t) e^{-j\omega t} dt \tag{52}$$

Over the interval $-\infty$ to ∞, the polynomial profile is piecewise. For a general polynomial profile with a rise of h and a rise time of t_r, the piecewise equation is given by:

$$x(t) = \begin{cases} 0 & t < 0 \\ s(t) & 0 \leq t \leq t_r \\ h & 1 < t_r \end{cases} \tag{53}$$

where

$$s(t) = C_0 + C_1 t + C_2 t^2 + \cdots + C_n t^n \tag{54}$$

The integral is separated into three intervals:

$$X(j\omega) = \int_{-\infty}^{0} 0 dt + \int_{0}^{t_r} s(t) e^{-j\omega t} dt + \int_{t_r}^{\infty} h e^{-j\omega t} dt \tag{55}$$

The integral is further expanded:

$$X(j\omega) = \int_{0}^{t_r} C_0 e^{-j\omega t} dt + \int_{0}^{t_r} C_1 t e^{-j\omega t} dt + \cdots \\ + \int_{0}^{t_r} C_n t^n e^{-j\omega t} dt + \int_{t_r}^{\infty} h e^{-j\omega t} \tag{56}$$

The integral containing C_n is expanded first using integration by parts:

$$\begin{aligned}\int_0^{t_r} C_n t^n e^{-j\omega t} dt = C_n e^{-j\omega t_r} \Bigg[& \left(\frac{j}{\omega}\right) (-1)^0 \left(\frac{n!}{(n-0)!}\right) t_r^n \\ & + \left(\frac{j}{\omega}\right)^2 (-1)^1 \left(\frac{n!}{(n-1)!}\right) t_r^{n-1} \\ & + \left(\frac{j}{\omega}\right)^3 (-1)^2 \left(\frac{n!}{(n-2)!}\right) t^{n-2} e^{-j\omega t} \\ & + \cdots \\ & + \left(\frac{j}{\omega}\right)^{n+1} (-1)^n \left(\frac{n!}{0!}\right) \Bigg] \\ & - \left(\frac{j}{\omega}\right)^{n+1} (-1)^n n! \end{aligned} \tag{57}$$

The next step is to use Euler's identity and separate terms into real and imaginary parts. If n is odd, then the expression becomes:

$$\begin{aligned}\int_0^{t_r} C_n t^n e^{-j\omega t} dt = C_n \big[& (a_n \cos \omega t_r + b_n \sin \omega t_r - d_n) \\ & + (b_n \cos \omega t_r - a_n \sin \omega t_r) j \big] \end{aligned} \tag{58}$$

where,

$$\begin{aligned} a_n = & \left(\frac{j}{\omega}\right)^2 (-1)^1 \left(\frac{n!}{(n-1)!}\right) t_r^{n-1} \\ & + \left(\frac{j}{\omega}\right)^4 (-1)^3 \left(\frac{n!}{(n-3)!}\right) t_r^{n-3} \\ & + \cdots \\ & + \left(\frac{j}{\omega}\right)^{n+1} (-1)^n \left(\frac{n!}{0!}\right) \end{aligned} \tag{59}$$

$$\begin{aligned} b_n = & \frac{1}{j} \left(\frac{j}{\omega}\right) (-1)^0 \left(\frac{n!}{(n-0)!}\right) t_r^n \\ & + \frac{1}{j} \left(\frac{j}{\omega}\right)^3 (-1)^2 \left(\frac{n!}{(n-2)!}\right) t_r^{n-2} \\ & + \cdots \\ & + \frac{1}{j} \left(\frac{j}{\omega}\right)^n (-1)^{n-1} \left(\frac{n!}{1!}\right) t_r \end{aligned} \tag{60}$$

$$d_n = \left(\frac{j}{\omega}\right)^{n+1} (-1)^n n! \tag{61}$$

The key components are the last terms in (59) and (61). This is where the quantity $1/\omega$ is raised to the $(n+1)^{th}$ power. It can be seen that the integrals in (56) with leading coefficients $C_0, C_1, \ldots, C_{n-1}$ cannot have the term $1/\omega$ raised to the $(n+1)^{th}$ power. Additionally, evaluating the last integral in (56) yields:

$$\int_{t_r}^{\infty} he^{-j\omega t} = \frac{-h}{\omega}(j\cos\omega t_r + \sin\omega t_r) \tag{62}$$

Therefore, the total CFT will contain one sine term, one cosine term, and one constant term with the quantity $1/\omega$ raised to the $(n+1)^{th}$ power. When the magnitude of the CFT is found, this quantity cannot be eliminated. The presence of this term is sufficient to show that the zeros of the CFT magnitude of any polynomial profile do not occur in a periodic manner.

If n is even, then (57) becomes:

$$\begin{aligned}\int_0^{t_r} C_n t^n e^{-j\omega t} dt = C_n \big[&(a_n \cos\omega t_r + b_n \sin\omega t_r) \\ &+ (b_n \cos\omega t_r - a_n \sin\omega t_r - d_n) j\big]\end{aligned} \tag{63}$$

where,

$$\begin{aligned} a_n = &\left(\frac{j}{\omega}\right)^2 (-1)^1 \left(\frac{n!}{(n-1)!}\right) t_r^{n-1} \\ &+ \left(\frac{j}{\omega}\right)^4 (-1)^3 \left(\frac{n!}{(n-3)!}\right) t_r^{n-3} \\ &+ \cdots \\ &+ \left(\frac{j}{\omega}\right)^n (-1)^{n-1} \left(\frac{n!}{0!}\right) \end{aligned} \tag{64}$$

$$\begin{aligned} b_n = &\frac{1}{j}\left(\frac{j}{\omega}\right) (-1)^0 \left(\frac{n!}{(n-0)!}\right) t_r^{n} \\ &+ \frac{1}{j}\left(\frac{j}{\omega}\right)^3 (-1)^2 \left(\frac{n!}{(n-2)!}\right) t_r^{n-2} \\ &+ \cdots \\ &+ \frac{1}{j}\left(\frac{j}{\omega}\right)^{n+1} (-1)^n \left(\frac{n!}{1!}\right) t_r \end{aligned} \tag{65}$$

$$d_n = \frac{1}{j}\left(\frac{j}{\omega}\right)^{n+1}(-1)^n n! \tag{66}$$

The same conclusion can be drawn when n is even.

APPENDIX C

SLOSHING SURFACE PLOTS

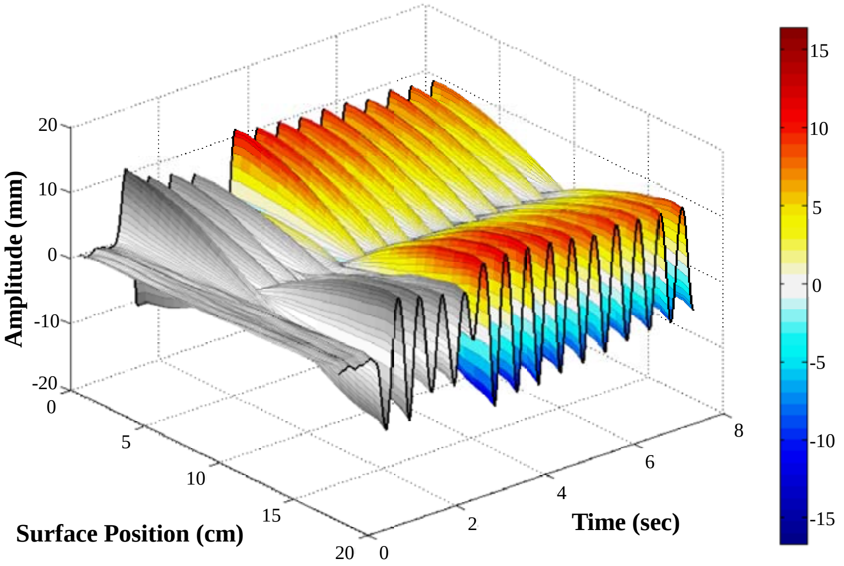

Figure 55. Surface Oscillations for 3-4-5 Polynomial Profile Case, 12 cm Liquid Depth

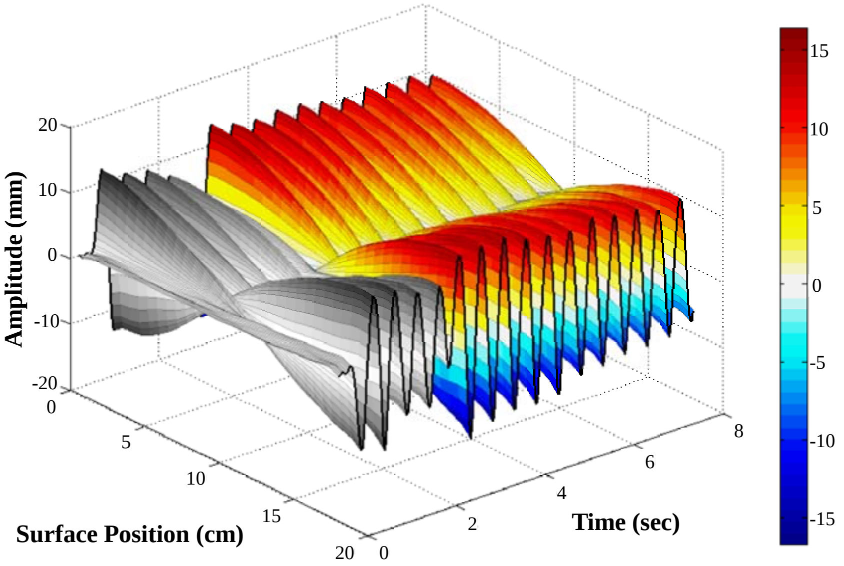

Figure 56. Surface Oscillations for 4-5-6-7 Polynomial Profile Case, 12 cm Liquid Depth

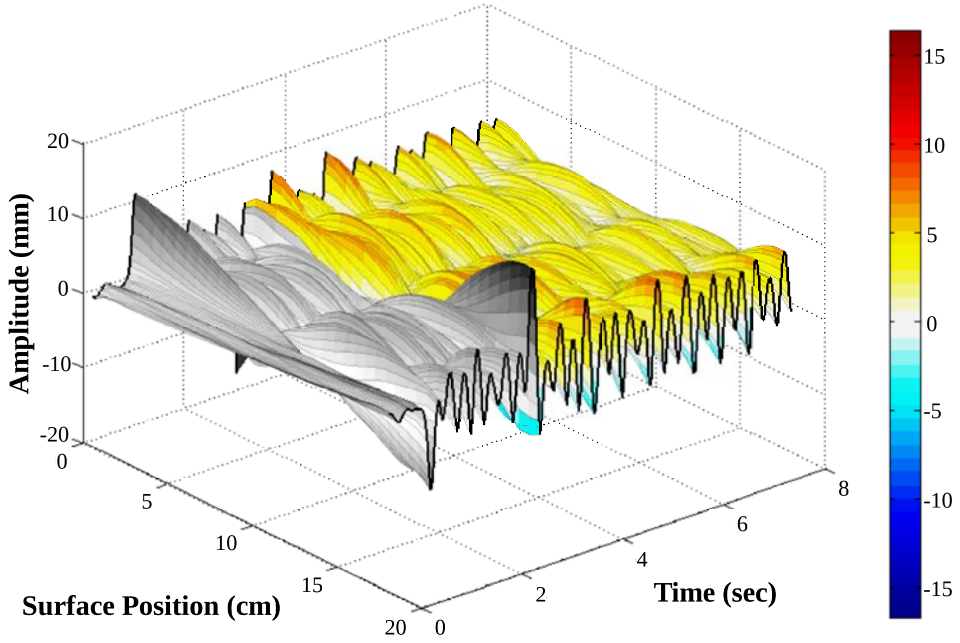

Figure 57. Surface Oscillations for ZV-Shaped Case, 12 cm Liquid Depth

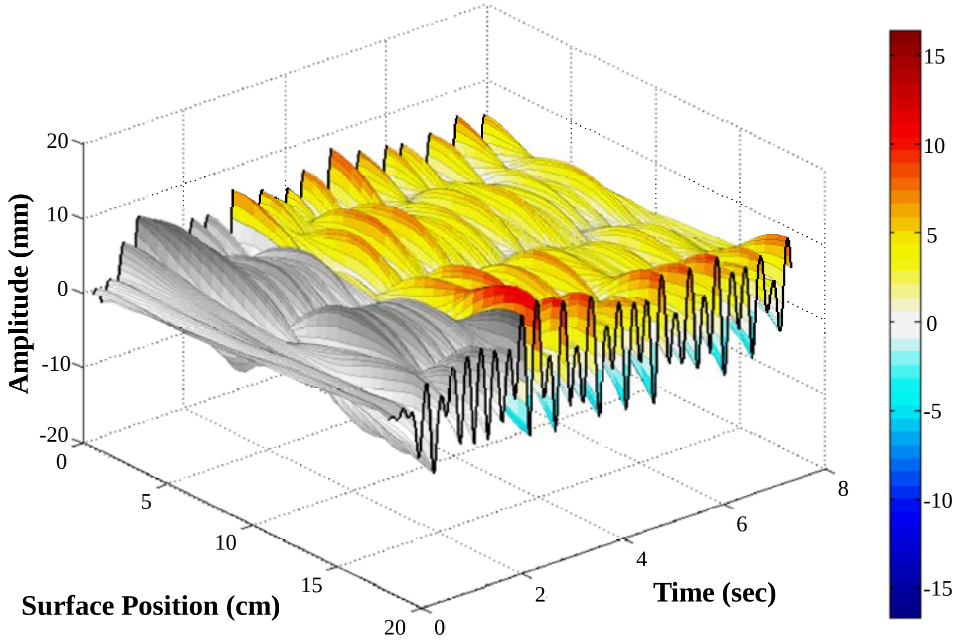

Figure 58. Surface Oscillations for EI-Shaped Case, 12 cm Liquid Depth

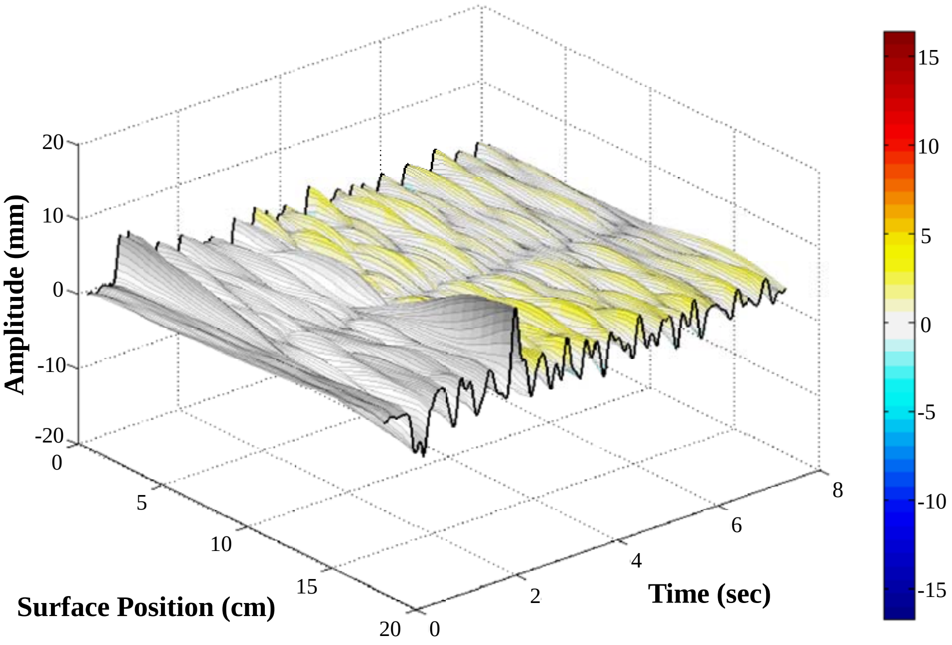

Figure 59. Surface Oscillations for ZV2M-Shaped Case, 12 cm Liquid Depth

REFERENCES

[1] ABDEL-RAHMAN, E. M., NAYFEH, A. H., and MASOUD, Z. N., "Dynamics and control of cranes: A review," *Journal of Vibration and Control*, vol. 9, pp. 893–908, July 2003.

[2] ABOEL-HASSAN, A., ARAFA, M., and NASSEF, A., "Design and optimization of input shapers for liquid slosh suppression," *Journal of Sound and Vibration*, vol. 320, pp. 1–15, 2009.

[3] ABRAMSON, H. N., "The dynamic behavior of liquids in moving containers," Tech. Rep. SP-106, NASA, 1966.

[4] ACARMAN, T. and OZGUNER, U., "Rollover prevention for heavy trucks using frequency shaped sliding mode control," *Vehicle System Dynamics*, vol. 44, no. 10, pp. 737 – 762, 2006.

[5] ANDRESEN, U. and SINGHOSE, W., "A simple procedure for modifying high-speed cam profiles for vibration reduction," *ASME J. of Mechanical Design*, vol. 126, pp. 1105–08, 2004.

[6] ASPINWALL, D. M., "Acceleration profiles for minimizing residual response," *ASME Journal of Dynamic Systems, Measurement, and Control*, vol. 102, pp. 3–6, March 1980.

[7] BANDYOPADHYAY, B., GANDHI, P., and KURODE, S., "Sliding mode observer based sliding mode controller for slosh-free motion through pid scheme," *IEEE Transactions on Industrial Electronics*, vol. 56, pp. 3432 –3442, September 2009.

[8] CHEN, F. Y., *Mechanics and Design of Cam Mechanisms*. Pergamon Pr, 1982.

[9] CHEN, K.-S. and OU, K.-S., "Simulations and experimental investigations on residual vibration suppression of electromagnetically actuated structures using command shaping methods," *Journal of Vibration and Control*, vol. 16, pp. 1713–1734, Oct 2010.

[10] CHEN, S., HEIN, B., and WORN, H., "Using acceleration compensation to reduce liquid surface oscillation during a high speed transfer," in *IEEE International Conference on Robotics and Automation*, pp. 2951–2956, April 2007.

[11] CHEW, M. and CHUANG, C. H., "Minimizing residual vibrations in high-speed cam-follower systems over a range of speeds," *Journal of Mechanical Design*, vol. 117, pp. 166–172, 1995.

[12] D. D. FUJIOKA, A. RAUCH, W. S. and JONES, T., "Tip-over stability analysis of mobile boom cranes with double-pendulum payloads," in *American Control Conference*, 2009.

[13] DODGE, F. T., "The new 'Dynamic behavior of liquids in moving containers'," tech. rep., Southwest Research Institute, 2000.

[14] ELOUNDOU, R. and SINGHOSE, W., "Interpretation of s-curve reference commands as input-shaped functions," in *American Control Conference*, (Anchorage, AK), 2002.

[15] ERKORKMAZ, K. and ALTINTAS, Y., "Quintic spline interpolation with minimal feed fluctuation," *Journal of Manufacturing Science and Engineering*, vol. 127, no. 2, pp. 339–349, 2005.

[16] FEDDEMA, J. T., DOHRMANN, C. R., PARKER, G. G., ROBINETT, R. D., and ROMERO, VINCENTE J.AND SCHMITT, D. J., "Control for slosh-free motion of an open container," *IEEE Control Systems*, pp. 29–36, 1997.

[17] FLOCKER, F. W., "Controlling the frequency content of inertia forces in dwelling cam-follower systems," *Journal of Mechanical Design*, vol. 129, no. 5, pp. 546–552, 2007.

[18] GANDHI, P. S., JOSHI, K. B., and ANANTHKRISHNAN, N., "Design and development of a novel 2DOF actuation slosh rig," *Journal of Dynamic Systems, Measurement, and Control*, vol. 131, no. 1, pp. 011006–1–011006–9, 2009.

[19] GLOSSIOTIS, G. and ANTONIADIS, I., "Digital filter based motion command preconditioning of time varying suspended loads in boom cranes for sway suppression," *Journal of Vibration and Control*, vol. 13, pp. 617–656, May 2007.

[20] GOSSELIN, C. M. and HADJ-MESSAOUD, A., "Automatic planning of smooth trajectories for pick-and-place operations," *Journal of Mechanical Design*, vol. 115, no. 3, pp. 450–456, 1993.

[21] GRUNDELIUS, M. and BERNHARDSSON, B., "Constrained iterative learning control of liquid slosh in an industrial packaging machine," in *39th IEEE Conference on Decision and Control*, vol. 5, pp. 4544 –4549, 2000.

[22] HAMAGUCHI, M., YOSHIDA, Y., KIHARA, T., and TANIGUCHI, T., "Path design and trace control of a wheeled mobile robot to damp liquid sloshing in a cylindrical container," in *IEEE International Conference on Mechatronics and Automation*, vol. 4, pp. 1959 – 1964, July-1 Aug. 2005.

[23] HARA, F., "Refined active control of sloshing by intermittent gas-bubble injection," in *First International Conference on Motion and Vibration Control*, pp. 1104–1109, September 1992.

[24] HUNG, R. J., LONG, Y. T., and CHI, Y. M., "Slosh dynamics coupled with spacecraft attitude dynamics. i - formulation and theory," *AIAA Journal of Spacecraft and Rockets*, vol. 33, no. 4, pp. 582–593, 1996.

[25] HUNG, R. J., LONG, Y. T., and CHI, Y. M., "Slosh dynamics coupled with spacecraft attitude dynamics. ii - orbital environment application," *AIAA Journal of Spacecraft and Rockets*, vol. 33, no. 4, pp. 582–593, 1996.

[26] HUNG, R. J. and PAN, H. L., "Sloshing-induced moment driven by gravity gradient associated with spacecraft slew motion," *AIAA Journal of Spacecraft and Rockets*, vol. 32, no. 5, pp. 817–824, 1995.

[27] HYDE, J. and SEERING, W., "Using input command pre-shaping to suppress multiple mode vibration," in *IEEE Int. Conf. on Robotics and Automation*, (Sacramento, CA), pp. 2604–2609, 1991.

[28] IBRAHIM, R. A., PILIPCHUK, V. N., and IKEDA, T., "Recent advances in liquid sloshing dynamics," *Applied Mechanics Reviews*, vol. 54, no. 2, 2001.

[29] KOMOGUCHI, Y., KUNIEDA, M., and YANO, K., "Liquid handling control for service robot by hybrid shape approach," in *SICE Annual Conference*, pp. 1737–1740, August 2008.

[30] KURODE, S., BANDYOPADHYAY, B., and GANDHI, P., "Sliding mode control for slosh-free motion of a container using partial feedback linearization," in *International Workshop on variable Structure Systems*, pp. 367 –372, June 2008.

[31] LAWRENCE, J. and SINGHOSE, W., "Design of minicrane for education and research," in *6th Int. Conference on Research and Education in Mechatronics*, (Annecy, France), 2005.

[32] LI, H., LE, M., GONG, Z., and LIN, W., "Motion profile design to reduce residual vibration of high-speed positioning stages," *IEEE/ASME Transactions on Mechatronics*, vol. 14, pp. 264 –269, April 2009.

[33] MECKL, P. H., ARESTIDES, P. B., and WOODS, M. C., "Optimized s-curve motion profiles for minimum residual vibration," in *American Control Conference*, (Philadelphia, PA), 1998.

[34] MIDHA, A. and TURCIC, D. A., "On the periodic response of cam mechanism with flexible follower and camshaft," *Journal of Dynamic Systems, Measurement, and Control*, vol. 102, no. 4, pp. 255–264, 1980.

[35] MOULIN, H. and BAYO, E., "On the accuracy of endpoint trajectory tracking for flexible arms by non-causal inverse dynamic solution," *ASME Journal of Dynamic Systems, Measurement and Control*, vol. 113, pp. 320–324, 1991.

[36] MUTO, K., KASAI, Y., and NAKAHARA, M., "Experimental tests for suppression effects of water restraint plates in sloshing of a water pool," *Journal of Pressure Vessel Technology*, vol. 110, pp. 240–246, 1988.

[37] NODA, Y., YANO, K., HORIHATA, S., and TERASHIMA, K., "Sloshing suppression control during liquid container transfer involving dynamic tilting using Wigner distribution analysis," in *43rd IEEE Conference on Decision and Control*, vol. 3, pp. 3045 – 3052 Vol.3, December 2004.

[38] NORTON, R. L., *Cam Design and Manufacturing Handbook.* Industrial Press, Inc., 2002.

[39] OH, C., SUN, B., PARK, Y., and ROH, W., "Sloshing analysis using ground experimental apparatus," in *International Conference on Control, Automation and Systems*, pp. 2203–2207, October 14-17 2008.

[40] PARK, J. Y. and CHANG, P. H., "Vibration control of a telescopic handler using time delay control and commandless input shaping technique," *Control Engineering Practice*, vol. 12, no. 6, pp. 769–780, 2004.

[41] PARK, U. H., LEE, J. W., LIM, B. D., and SUNG, Y. G., "Design and sensitivity analysis of an input shaping filter in the z-plane," *J. of Sound and Vibration*, vol. 243, pp. 157–171, 2001.

[42] PENG, K. C. C. and SINGHOSE, W., "Crane control using machine vision and wand following," in *IEEE International Conference on Mechatronics*, (Malaga, Spain), 2009.

[43] PERTERSON, L. D., CRAWLEY, E. F., and HANSMAN, R. J., "Nonlinear fluid slosh coupled to the dynamics of spacecraft," *AIAA Journal*, vol. 27, no. 9, pp. 1230–1240, 1989.

[44] PIAZZI, A. and VISIOLI, A., "Minimum-time system-inversion-based motion planning for residual vibration reduction," *IEEE/ASME Transactions on Mechatronics*, vol. 5, no. 1, pp. 12 –22, 2000.

[45] QI, N., DONG, K., WANG, X., and LI, Y., "Spacecraft propellant sloshing suppression using input shaping technique," pp. 162 –166, Feb. 2009.

[46] QUADRELLI, M., "Nutation time constant determination of on-axis diaphragm tanks on spinner spacecraft," *AIAA Journal of Spacecraft and Rockets*, vol. 42, no. 3, pp. 530–542, 2005.

[47] RAMOS, F., FELIU, V., and PAYO, I., "Design of trajectories with physical constraints for very lightweight single link flexible arms," *Journal of Vibration and Control*, vol. 14, pp. 1091–1110, Aug 2008.

[48] RAUCH, A. and SINGHOSE, W., "Stability analysis of mobile boom cranes," in *International Conference on Motion and Vibration Control*, 2008.

[49] ROBERTS, J. R., BASURTO, E. R., and CHEN, P.-Y., "Slosh design handbook I," Tech. Rep. CR-406, NASA, 1966.

[50] ROTHBART, H. A., *Cam Design Handbook.* The McGraw-Hill Companies, Inc., 2004.

[51] SINGER, N. C. and SEERING, W. P., "Preshaping command inputs to reduce system vibration," *J. of Dynamic Sys., Measurement, and Control*, vol. 112, pp. 76–82, 1990.

[52] SINGER, N. C., SINGHOSE, W. E., and SEERING, W. P., "Comparison of filtering methods for reducing residual vibration," *European Journal of Control*, no. 5, pp. 208–218, 1999.

[53] SINGHOSE, W., "Command shaping for flexible systems: A review of the first 50 years," *International Journal of Precision Engineering and Manufacturing*, vol. 10, no. 4, pp. 153–168, 2009.

[54] SINGHOSE, W. and SEERING, W., *Command Generation for Dynamic Systems.* www.lulu.com/content/621219. 978-0-9842210-0-4, 2010.

[55] SINGHOSE, W. and VAUGHAN, J., "Reducing vibration by digital filtering and input shaping," *IEEE Transactions on Control Systems Technology*, vol. PP, no. 99, p. 1, 2010.

[56] SINGHOSE, W., ELOUNDOU, R., and LAWRENCE, J., "Command generation for flexible systems by input shaping and command smoothing," *AIAA Journal of Guidance, Control, and Dynamics*, vol. 33, no. 6, 2010.

[57] SINGHOSE, W., KIM, D., and KENISON, M., "Input shaping control of double-pendulum bridge crane oscillations," *ASME J. of Dynamic Systems, Measurement, and Control*, vol. 130, May 2008.

[58] SINGHOSE, W., SEERING, W., and SINGER, N., "Residual vibration reduction using vector diagrams to generate shaped inputs," *ASME J. of Mechanical Design*, vol. 116, no. June, pp. 654–659, 1994.

[59] SINGHOSE, W., SEERING, W., and SINGER, N., "Input shaping for vibration reduction with specified insensitivity to modeling errors," in *Japan-USA Sym. on Flexible Automation*, vol. 1, (Boston, MA), pp. 307–13, 1996.

[60] SINGHOSE, W., SINGER, N., and SEERING, W., "Time-optimal negative input shapers," *ASME J. of Dynamic Systems, Measurement, and Control*, vol. 119, no. June, pp. 198–205, 1997.

[61] SIRA-RAMIREZ, H. and FLIESS, M., "A flatness based generalized PI control approach to liquid sloshing regulation in a moving container," in *American Control Conference*, vol. 4, pp. 2909 – 2914, 2002.

[62] SMITH, O. J. M., *Feedback Control Systems*. New York: McGraw-Hill Book Co., Inc., 1958.

[63] SRINIVASAN, L. N. and GE, Q. J., "Designing dynamically compensated and robust cam profiles with Bernstein-Bézier harmonic curves," *Journal of Mechanical Design*, vol. 120, no. 1, pp. 40–45, 1998.

[64] SUK, J. and KIM, Y., "Experimental evaluation of the torque-shaping method for slew maneuver of flexible space structures," *Journal of Guidance, Control, and Dynamics*, vol. 21, no. 6, pp. 817–822, 1998.

[65] SWIGERT, C. J., "Shaped torque techniques," *Journal of Guidance and Control*, vol. 3, no. 5, pp. 460–467, 1980.

[66] TERASHIMA, K., HAMAGUCHI, M., and YANO, K., "Modeling and input shaping control of liquid vibration for an automatic pouring system," in *35th IEEE Conference on Decision and Control*, pp. 4844–4850, 1996.

[67] TERASHIMA, K. and SCHMIDT, G., "Motion control of a cart-based container considering suppression of liquid oscillations," in *IEEE International Symposium on Industrial Electronics*, pp. 275 –280, May 1994.

[68] TERASHIMA, K. and YANO, K., "Sloshing analysis and suppression control of tilting-type automatic pouring machine," *Control Engineering Practice*, vol. 9, no. 6, pp. 607 – 620, 2001.

[69] UTSUMI, M., "Low-gravity slosh analysis for cylindrical tanks with hemiellipsoidal top and bottom," *AIAA Journal of Spacecraft and Rockets*, vol. 45, no. 4, pp. 813–821, 2008.

[70] UTSUMI, M., "Slosh analysis for teardrop tank," *AIAA Journal of Spacecraft and Rockets*, vol. 45, no. 5, pp. 1053–1060, 2008.

[71] VACLAVIK, M. and JIRASKO, P., "Research and application of displacement laws of electronic cams," in *12th IFToMM World Congress*, (Besancon, France), 2007.

[72] VENUGOPAL, R. and BERNSTEIN, D. S., "State space modeling and active control of slosh," in *IEEE International Conference on Control Applications*, pp. 1072 –1077, September 1996.

[73] WANG, J. and TSAO, T.-C., "Repetitive control of linear time varying systems with application to electronic cam motion control," June 30 - July 2 2004.

[74] WIEDERRICH, J. L. and ROTH, B., "Dynamic synthesis of cams using finite trigonometric series," *ASME Journal of Engineering for Industry*, pp. 287–293, Feb. 1975.

[75] YANG, D. C. H. and WANG, F.-C., "A quintic spline interpolator for motion command generation of computer-controlled machines," *Journal of Mechanical Design*, vol. 116, no. 1, pp. 226–231, 1994.

[76] YANG, J., KIM, J., PITARCH, E. P., and ABDEL-MALEK, K., “Optimal trajectory planning for redundant manipulators based on minimum jerk,” in *32nd Mechanisms and Robotics Conference*, vol. 2008, (Brooklyn, NY), pp. 1141–1150, 2008.

[77] YANO, K. and TERASHIMA, K., “Sloshing suppresion control of liquid transfer systems considering a 3-d transfer path,” *IEEE/ASME Transactions on Mechatronics*, vol. 20, no. 1, pp. 8–16, 2005.

[78] YANO, K., TODA, T., and TERASHIMA, K., “Sloshing suppression control of automatic pouring robot by hybrid shape approach,” in *40th IEEE Conference on Decision and Control*, vol. 2, pp. 1328 –1333, 2001.

[79] YANO, K. and TERASHIMA, K., “Robust liquid container transfer control for complete sloshing suppression,” *IEEE Transactions on Control Systems Technology*, vol. 9, pp. 483 –493, May 2001.

[80] YOON, K. and RAO, S. S., “Cam motion synthesis using cubic splines,” *Journal of Mechanical Design*, vol. 115, no. 3, pp. 441–446, 1993.

[81] YU, Q. and LEE, H. P., “A new family of parameterized polynomials for cam motion synthesis,” *Journal of Mechanical Design*, vol. 117, no. 4, pp. 653–655, 1995.

[82] YU, Q. and LEE, H. P., “Influence of cam motions on the dynamic behavior of return springs,” *Journal of Mechanical Design*, vol. 120, no. 2, pp. 305–310, 1998.

[83] ZANASI, R. and MORSELLI, R., “Third order trajectory generator satisfying velocity, acceleration and jerk constraints,” in *International Conference on Control Applications*, vol. 2, pp. 1165 – 1170, 2002.

[84] ZIMMERT, N., KHARITONOV, A., and SAWODNY, O., “A new control strategy for trajectory tracking of fire-rescue turntable ladders,” in *17th World Congress, International Federation of Automatic Control*, vol. 17, July 2008.

[85] ZIMMERT, N. and SAWODNY, O., “A trajectory tracking control with disturbance-observer of a fire-rescue turntable ladder,” in *American Control Conference*, pp. 4041 –4046, June 2008.